REVIEW ARTICLE | APRIL 10 2025

Boron nitride nanosheets, quantum dots, and dots: Synthesis, properties, and biomedical applications

Special Collection: 2D Materials for Biomedical Applications

Raksha Dubey ; Matthew Cowles; Zohreh Salimi; Xiuling Liu; Rodney Oakley; Nazmiye Yapici; Join Uddin ; Dongyan Zhang ; Yoke Khin Yap

APL Mater. 13, 040601 (2025)
https://doi.org/10.1063/5.0255590
CHORUS

APL Materials REVIEW pubs.aip.org/aip/apm

Boron nitride nanosheets, quantum dots, and dots: Synthesis, properties, and biomedical applications

Cite as: APL Mater. 13, 040601 (2025); doi: 10.1063/5.0255590
Submitted: 30 December 2024 • Accepted: 14 February 2025 •
Published Online: 10 April 2025

Raksha Dubey,[1] Matthew Cowles,[1,2] Zohreh Salimi,[1] Xiuling Liu,[1,2] Rodney Oakley,[2] Nazmiye Yapici,[1,2] Join Uddin,[1] Dongyan Zhang,[1] and Yoke Khin Yap[1,a)]

AFFILIATIONS

[1] Department of Physics, and Elizabeth and Richard Henes Center for Quantum Phenomena, Michigan Technological University, 1400 Townsend Drive, Houghton, Michigan 49931, USA
[2] StabiLux Biosciences, Inc., 600 S. Wagner Rd., Ann Arbor, Michigan 48103, USA

Note: This paper is part of the Special Topic on 2D Materials for Biomedical Applications.
[a)] **Author to whom correspondence should be addressed:** ykyap@mtu.edu

ABSTRACT

This review examines three aspects of hexagonal boron nitride (h-BN) nanomaterials: properties, synthesis methods, and biomedical applications. We focus the scope of review on three types of h-BN nanostructures: boron nitride nanosheets (BNNSs, few-layered h-BN, larger than ~100 nm in lateral dimensions), boron nitride quantum dots (BN QDs, smaller than ~10 nm in all dimensions, with inherent excitation-dependent fluorescence), and boron nitride dots (BN dots, smaller than ~10 nm in all dimensions, wide bandgap without noise fluorescence). The synthesis methods of BNNSs, BN QDs, and BN dots are summarized in top-down and bottom-up approaches. Future synthesis research should focus on the scalability and the quality of the products, which are essential for reproducible applications. Regarding biomedical applications, BNNSs were used as nanocarriers for drug delivery, mechanical reinforcements (bone tissue engineering), and antibacterial applications. BN QDs are still limited for non-specific bioimaging applications. BN dots are used for the small dimension to construct high-brightness probes (HBPs) for gene sequence detections inside cells. To differentiate from other two-dimensional materials, future applications should focus on using the unique properties of BN nanostructures, such as piezoelectricity, boron neutron capture therapy (BNCT), and their electrically insulating and optically transparent nature. Examples would be combining BNCT and chemo drug delivery using BNNSs, and using BN dots to form HBPs with enhanced fluorescence by preventing fluorescence quenching using electrically insulating BN dots.

I. INTRODUCTION

Boron nitride nanosheets (BNNSs)[1–4] are thin (few-layered) hexagonal phase boron nitride (h-BN) crystals. They are electrically insulating two-dimensional (2D) materials, different from the electrically conducting graphene[5] and semiconducting transition metal dichalcogenides (TMDs).[6,7] BNNSs are structurally similar to graphene and consist of h-BN layers held by van der Waals (vdW) forces. BNNSs can appear as boron nitride quantum dots (BN QDs)[8–12] and BN dots[13] when their lateral dimensions are below ~10 nm, as schematically represented in Fig. 1.

BNNSs are thin h-BN with lateral sizes larger than hundreds of nm. Therefore, BNNSs are electrically insulating with wide energy bandgaps (~6 eV), just like h-BN. In contrast, BN QDs synthesized thus far are below ~10 nm in lateral dimensions and emit a wide range of fluorescence across the visible optical spectra. BN QDs' fluorescence is excitation-dependent, emitting light from ~400 to 550 nm as excited at ~350–500 nm. The origins of such a diverse emission nature are likely due to impurities and defects of the nanoscale h-BN particles.[9,10] Initial calculations suggest that the highest occupied molecular orbital (HOMO)–lowest unoccupied molecular orbital (LUMO) gap of BN QDs can be larger than that

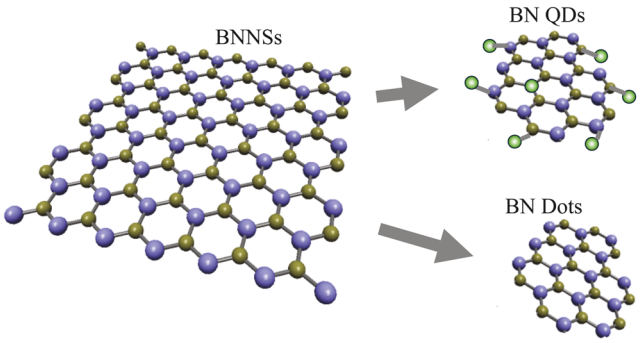

FIG. 1. Schematic illustration of BNNSs, BN QDs, and BN Dots.

of monolayer (ML) BNNSs and varied by size and shape (HOMO: highest occupied molecular orbital and LUMO: lowest unoccupied molecular orbital).[8] However, almost all the synthesized BN QDs behaved differently, with optical bandgaps much smaller than monolayer BNNSs. It is strange to have named these BN nanoparticles QDs, as their optical properties have nothing to do with quantum confinement effects.

More recently, Yap *et al.* reported a new class of BN dots.[13] BN dots differ from BN QDs as they are not fluorescent. The properties of BN dots are like BNNSs with a ~6 eV bandgap and no quantum confinement effect; therefore, they are named "dots." In gene sequence detection, BN dots can be zero-dimensional carriers for high-brightness probes (HBPs).[13] In particular, Yap *et al.* could conjugate a series of organic dye molecules on each BN dot, enabling high-brightness fluorescent probes (HBPs) that could target gene sequences when conjugated with oligonucleotides (Oligos) or single-stranded deoxyribonucleic acids (ssDNAs).

This article reviews the synthesis, characterization, and biomedical application of BNNSs, BN QDs, and BN dots. Section II briefly reviews these nanoscale BN materials' structural and optical properties. Section III summarizes the synthesis method of BNNSs, BN QDs, and BN dots. Section IV discusses the biomedical application of BNNSs, BN QDs, and BN dots. Finally, Sec. V elaborates on the future perspective of BNNSs, BN QDs, and BN dots for biomedical applications.

II. PROPERTIES OF BNNSs, BN QDs, AND BN DOTS

Boron nitride (BN)[14,15] appears in multiple phases, including cubic (c-BN), hexagonal (h-BN), wurtzite (w-BN), rhombohedral (r-BN), and nanotubes (BNNTs). There has been an increased interest in boron nitride research due to the structural similarity with the carbon phases, such as graphene and carbon nanotubes. In the past, c-BN has gained much attention for its superhard properties for mechanical applications. Scientists have invested in tremendous studies to synthesize c-BN thin films and avoid h-BN formation. Interestingly, the situation reversed after discovering graphene. 2D h-BN, i.e., BNNSs, are now popular for research and applications for their high mechanical strength, thermal conductivity, chemical inertness, high-temperature resistance, and electrically insulating nature, all attributed to their strong covalent sp^2 bonds and ~6 eV bandgap.[16,17]

A. Properties of boron nitride nanosheets (BNNSs)

The band structure calculation in 1976 suggests that 2D h-BN has a direct optical gap of 5.8 eV and reasonably matches experimental values.[18] Theoretically, the average B–N bond length is ~1.43 Å.[19] The length of BNNSs is very similar to the C–C bond length in graphene. Electrons are known to be localized near the N atoms in B–N bonds,[19] with N atoms contributing to the valence band and B atoms contributing to the conduction band.[20] Density functional theory suggests that changing the strain from −10% to 10% lowered the bandgap of BNNSs,[21] consistent with our earlier report by Zhong *et al.*[19]

Experimentally, BNNSs could also be synthesized by chemical vapor deposition (CVD). The properties of CVD BNNSs are shown

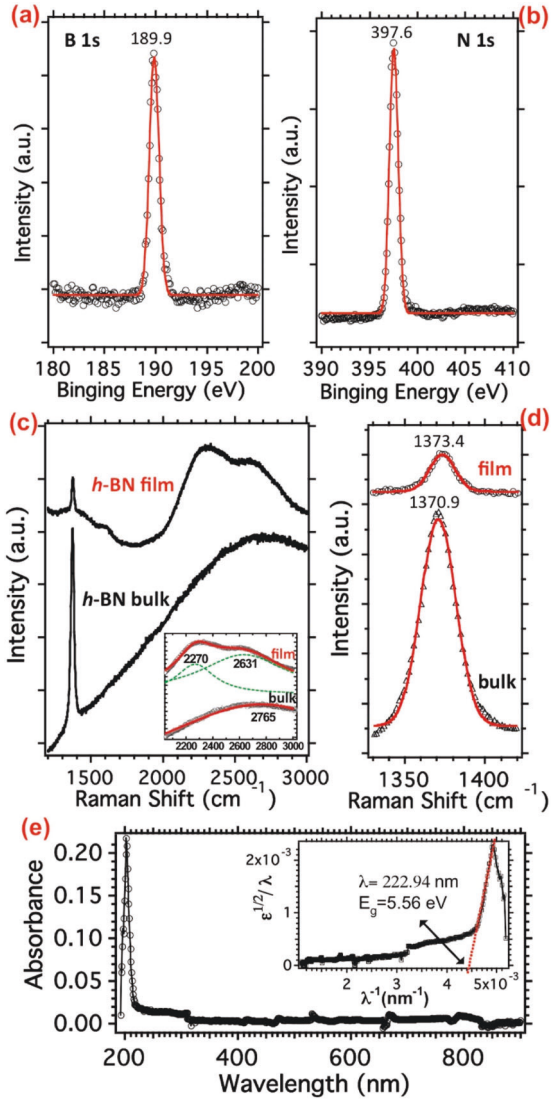

FIG. 2. XPS [(a) and (b)], Raman [(c) and (d)], and UV–Vis (e) spectra of CVD BNNSs. Reproduced with permission from Splendiani *et al.*, Nano Lett. **10**(4), 1271–1275 (2010). Copyright 2010 American Chemical Society.

in Fig. 2. For instance, the B 1s and N 1s binding energies measured by x-ray photoelectron spectroscopy (XPS) show peaks at 189.9 and 397.6 eV, respectively.[3] BNNSs can be determined by an E_{2g} Raman scattering peak around 1373 vs 1371 cm^{-1} from bulk h-BN. The optical bandgap for CVD BNNSs is estimated at 5.56 eV.

B. Properties of boron nitride quantum dots (BN QDs)

BN QDs were calculated in 2011 with triangular and hexagonal shapes.[8] At n = 3 (number of hexagons at the edges), the HOMO–LUMO gaps of BN QDs are larger than that of monolayered BNNSs. BN QDs were synthesized in 2014[9,10] and emit fluorescence in the visible spectra, suggesting that the optical gaps are smaller than those of BNNSs. Such optical properties are not due to quantum confinement effects and were attributed to defects and impurities. BN QDs initiate weak Raman scattering around 1365–1367 cm^{-1}.

Figure 3 shows the typical infrared (IR), XPS, and fluorescent spectra of these BN QDs. As shown in (a), BN QDs are not pure h-BN and contain –OH, carbon, and oxygen bonds, consistent with the XPS elemental data (b). BN QDs show excitation-dependent emissions, where the fluorescent wavelengths depend on the excitation wavelengths (c).

C. Properties of boron nitride dots (BN dots)

The as-synthesized BN dots exhibit excitation-dependent emissions like BN QDs. After removing the impurities and passivating the defects, BN dots could be treated as purified BN QDs that suppress excitation-dependent emissions. Therefore, BN dots can be used as nanocarriers for further chemical conjugation in biomedical applications.[13] As shown in Fig. 4, the as-synthesized BN dots (pristine carriers, much like BN QDs) have a broad fluorescence. After acid washing, the fluorescence (processed carriers) is suppressed as the impurities are removed. The fluorescence becomes ignorable after covalent conjugation with polyethylene glycol (PEG) linkers (processed carriers with linkers). As shown, subsequent conjugation with fluorescein (FAM) dye molecules leads to the desired green fluorescence.

III. SYNTHESIS TECHNIQUES OF BNNSs AND BN QDs

The two synthesis paths for nanoparticles are top-down and bottom-up production. Top-down synthesis implies the fracturing or exfoliation of larger particles into smaller ones, while bottom-up processes involve the creation of particles by employing molecular, ionic, or atomic precursors. Top-down production tends to supply low yields of BN QDs, while bottom-up methods are prone to heavy contamination from the precursors or additives.

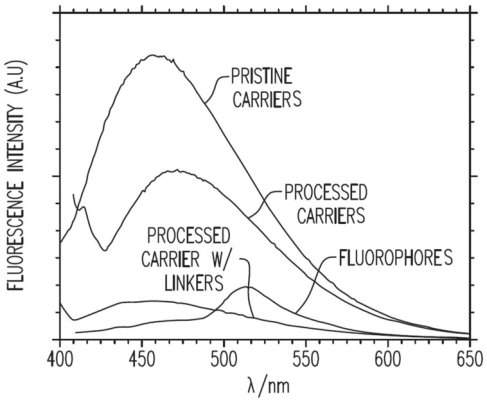

FIG. 4. Fluorescent spectra of as-synthesized BN dots (pristine carriers), processed carriers, processed carriers with linkers, and after conjugation with FAM dye molecules (fluorophores).[13] Intensities are not on the same scale for best visibility.

A. Top-down methods

Traditional top-down methods can be classified as mechanical, chemical, or mechano-chemical exfoliation. Although these have been mostly abandoned in favor of chemically assisted synthesis techniques, the most popular mechanical methods include wet and dry milling.[22] Milling relies on generating compression and shear forces to fracture h-BN, often accompanied by brief sonication. The yield of BNNSs can be increased by including intercalating (i.e., ammonia-borane[23]) or lubricating agents[24–27] in the process to aid in exfoliation, prevent re-aggregation, and increase the shear force.[22] In addition, the inclusion of boric acid[28] and sucrose[29] has led to BNNS yields of 89% and 87.3%, respectively, while being environmentally friendly and non-corrosive. It is possible to forgo the compression forces and wholly rely on generating large shear forces using high-pressure or rotor-stator equipment, such as a homogenizer or kitchen blender.[30–32] Purely mechanical methods may supply a

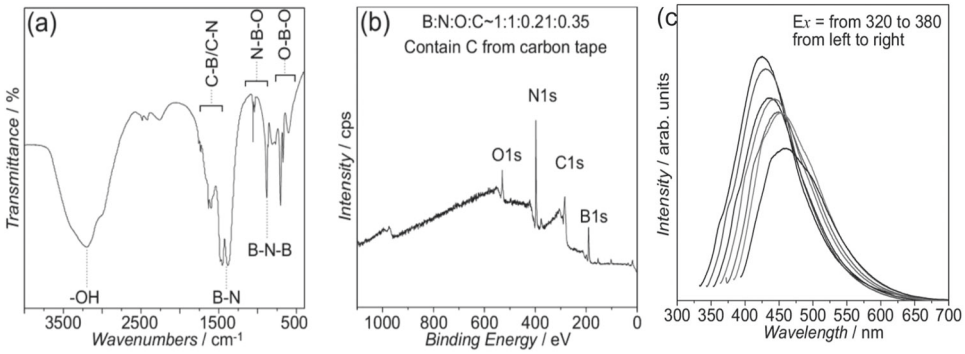

FIG. 3. Typical IR (a), XPS (b), and fluorescent (c) spectra of BN QDs. Reproduced with permission from Lin *et al.*, Small **10**(1), 60–65 (2014). Copyright 2013 Wiley-VCH Verlag GmbH & Co. KGaA.

very high yield of 2D structured materials but are generally ineffective at producing 0D nanoparticles with sufficient photoluminescent quantum yield (PL QY).

1. Liquid exfoliation

Liquid exfoliation is a simple method that relies on solvent properties to assist exfoliation[33] (Fig. 5), typically attempting to match the surface energy of h-BN and overcome vdW forces through polar solvents such as isopropyl alcohol (IPA), *N*,*N*-dimethylformamide (DMF), and *N*-methylpyrrolidone (NMP).[34–36] This method depends on the energy relationship between the solvent and layered material by adjusting for favorable interactions (e.g., dispersibility and polarity) and maximizing energy dispersivity, affected by solvent properties (e.g., density and polarity), particle dispersion, and energy input (e.g., shear forces, cavitation, and temperature).[37]

Although this is an important step in synthesizing QDs, liquid exfoliation is rarely the only step. For example, dispersing h-BN in DMF through ultrasonication before isolating the BNNSs through centrifugation led to a suspension that exhibited long-term stability, containing BNNSs that were semi-transparent under transmission electron microscopy (TEM) with lateral sizes greater than one micrometer,[38] agreeing with other findings;[39–41] further solvothermal processing was necessary for the synthesis of BN QDs. Fourier-transform infrared spectroscopy (FTIR) analysis of this sample exhibited B–N peaks at 1378 and 800 cm^{-1}, with methyl groups (2931 and 2857 cm^{-1}) that were attributed to surface functionalization by DMF degradants. However, this signal may also be caused by solvent adhesion between the BNNSs.[42] Chen *et al.* dispersed h-BN in a mixture of water, ethanol, and acetone to perform sonication-assisted liquid exfoliation.[40] The synthesized BNNSs were transparent and highly crystalline, with thicknesses around 3 nm. In addition to the liquid exfoliation, solvent degradation was assumed to produce hydroxyl groups that could effectively intercalate during ultrasonication, aiding in exfoliation before further solvothermal treatment to produce BN QDs. For example, Stengl *et al.* dispersed bulk powder in distilled water, IPA, or ethylene glycol (MEG) and subjected it to a high-intensity cavitation field before refluxing in MEG for 48 h.[10] XPS of the resulting BN QDs showed carbon and oxygen contamination much lower than traditional solvothermal methods.

2. Ionic intercalation

Ionic intercalation can be induced through several methods (vapor-phase, electrochemical, etc.),[43] but for BNNS/QD synthesis, it is mostly an extension of liquid phase exfoliation, operating through the dissociation of ions that self-insert between the layers of h-BN, increasing the relatively large interlayer distance of 0.33 nm[44] and weakening the vdWs force, maintaining h-BN's bulk structure.[34] Synthesis of BN QDs has been accomplished through the addition of hydrazine,[45] various acids,[10,41,46] and alkaline solutions.[9,39] Different intercalation materials can affect the surface state of the exfoliated h-BN by creating hydroxyl, amine,[45] or metaborate species for functionalization. Various examples include intercalating nickel and polylactic acid (PLA);[47] copper, gold, or silver;[48] and sodium hydroxide plus lithium chloride (LiCl), with Yu attributing a weight yield of 75.48% to the synergetic effect of cation intercalation and anion edge functionalization during high temperature/pressure (HTP) hydrothermal treatment.[49]

In some cases, reversible intercalation phases may be preferred. Kovtyukhova *et al.* explored the mechanisms driving ion intercalation to create reversible intercalation phases in bulk h-BN.[46] From the assortment of acids tested, evidence of intercalation was only achieved with phosphoric, sulfuric, and perchloric acids, with the d-spacing found to have increased by 0.36, 0.41, and 0.33 nm, respectively. No evidence of intercalation was found in the samples that were not heated until dry, with unique intercalation phases forming based on the heating and cooling cycles. Kumar *et al.* opted to use phosphoric acid to intercalate h-BN through high-intensity sonication.[41] Washing and centrifugation effectively separated the as-synthesized BN nanoplates and BN QDs. The BN nanoplates in the pellet underwent inhomogeneous thinning, where the edges appeared brighter than the centers under TEM, indicating fewer layers, as confirmed by high-resolution TEM (HRTEM) micrographs. The BN QDs in the supernatant exhibited lateral sizes of 3–6 nm and as few as 12 layers.

Yu[50] synthesized few-layer BNNSs (FL-hBN, 3–6 layers) using a similar method to Stengl.[10] Bulk h-BN, sulfuric acid, and potassium permanganate were chilled before stirring to homogeneity. Heating and cooling cycles with hydrogen peroxide and subsequent centrifugation, rinsing, and heated drying yielded high-quality BNNSs that appeared mostly transparent under TEM. By modifying the reaction temperatures and process time, they could control edge oxidation and produce FL-hBN nanosheets with the same crystallinity as h-BN with an average thickness of 1.78 nm and lateral sizes of around 486 nm. TEM mapping showed hydroxyl group functionalization on the edges of the BNNSs was much higher than in the center, indicating edge intercalation was enough to exfoliate thoroughly. This phenomenon can be seen in the elemental mapping in Fig. 6.

FIG. 5. Illustration depicting the synthesis of nanosheets through sonication and shear-assisted liquid-phase exfoliation followed by centrifugation to isolate the final product. Reproduced with permission from Hu *et al.*, Nanoscale **13**(2), 460–484 (2021). Copyright 2021 Royal Society of Chemistry.

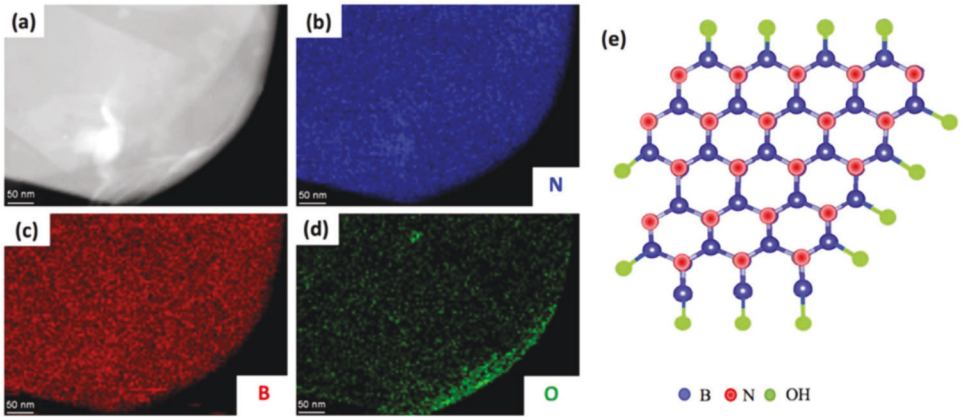

FIG. 6. TEM elemental mapping of few-layer h-BN nanosheets. (a) TEM image, (b) nitrogen, (c) boron, (d) oxygen, and (e) theoretical functionalization scheme of hydroxyl groups onto the 2D BN structure. Reproduced with permission from Yu *et al.*, Nanotechnology **32**(40), 405601 (2021). Copyright 2021 Institute of Physics.

Some debate exists about whether monatomic or more complex ions are preferred for ion intercalation.[44,51] The decomposition of intercalated compounds may be more efficacious than the continuous intercalation of stable atoms through subsequent processes. Furthermore, leftover ions can potentially affect the surface states of the exfoliating particles. Several major drawbacks to this method arise from the necessity for tedious neutralization steps and the tendency to produce QDs with low photoluminescence.[44,45] Liquid-phase ion intercalation is an environmentally friendly way to produce high-yield BNNSs with moderate edge functionalization. Still, it cannot be relied solely on for the mass production of highly luminescent BN QDs.

3. Hydrothermal and solvothermal

This has been a popular synthesis method for producing particles with higher QYs in an energy-efficient manner and with few ingredients. For example, Stengl *et al.* performed reflux solvothermal on BNNSs in MEG to synthesize BN QDs.[10] As schematically illustrated in Fig. 7, Li *et al.* subjected their BNNS suspension to HTP solvothermal processing for 24 h at 200 °C with filling factors of 40% and 66.7%,[38] yielding BN QDs with average lateral sizes of 3.19 and 3.46 nm, respectively. XPS spectra showed substantial carbon contamination and a significant reduction of the B 1s signal compared to the BNNSs. The BN QDs achieved a QY of up to 19.5%, exhibiting a pH-dependent PL response that indicates the BO_2^- species were mainly responsible for luminescent emissions. Traditional approaches for the solvothermal synthesis of BN QDs could only yield blue luminescence and low QY, while differences in solvent merely shifted the spectrum between blue and green PL.[45,52–54]

Given hydrothermal/solvothermal treatment's proclivity to facilitate significant amounts of contamination, Ding's group attempted to control the reactions that can occur to the surface state of BN QDs.[55] Building on past work,[29,56] various solvents were combined with specific passivating agents to control functionality and limit the types of defects capable of forming. By adding urea to the h-BN/NMP mixture, Ding could synthesize blue luminescent BN QDs with a size of 15 nm, a QY of 32.27%, and relatively low oxygen and carbon impurities compared to previously discussed work. In addition to their blue QDs, Ding *et al.* modified the solvent and passivating materials to yield yellow–green and red luminescent QDs. Density functional theory was used to determine that amine species prefer binding to the oxygen in the BO_x^- or the boron directly, leading to QD edges dominated by NH_2 functional groups;

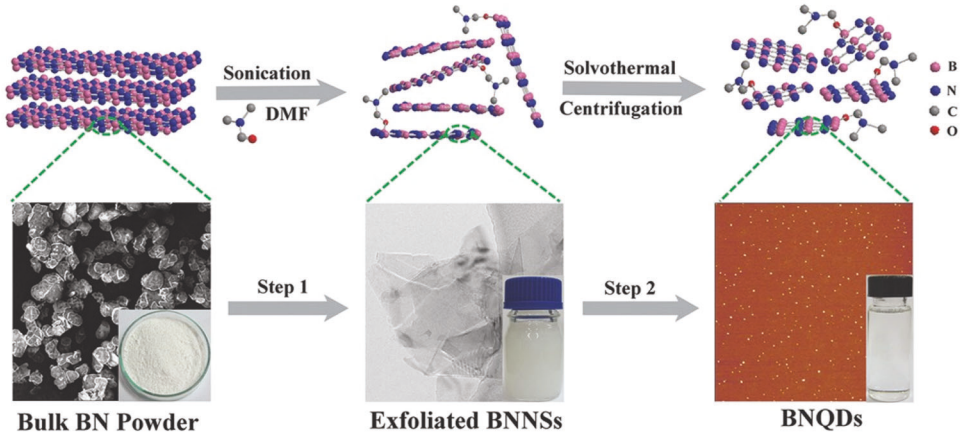

FIG. 7. Schematic illustration of the solvothermal method in producing BN QDs. Reproduced with permission from Li *et al.*, Small **11**(48), 6491–6499 (2015), Copyright 2015 Wiley-VCH Verlag GmbH & Co. KGaA.

this reaction enthalpy calculation was used to explain the extremely high PL emission in the blue BN QDs. Attempting to reproduce Ding's result, Wang used ethyl alcohol (EtOH) passivated with *p*-phenylenediamine to synthesize BN QDs through sonication and HTP solvothermal treatment.[57] These BN QDs had an average size of 4.9 nm, while XPS showed low amounts of carbon and oxygen bonding in the B 1s and N 1s peaks compared to the B–N signals. However, the sample was found to be 64.74% carbon with a substantial C 1s peak.

While solvothermal treatment is widely used to create BN QDs with high QY, XPS spectra tend to reveal predominant C and O 1s peaks compared to B and N 1s. While the specific mechanisms for PL emission or fluorescence are unclear, Ding and others have shown that targeting specific functional groups can effectively tune the emission wavelengths while limiting undesired impurities.[55]

4. Laser ablation in liquid (LAL)

Laser ablation is a high-energy approach to catalyzing reactions by relying on the condensation rate of growth vapors after exiting the direct beam path. Hydrothermal and ablation methods can be combined to produce nanomaterials by excluding a stationary reaction site that catalyzes spontaneous deposition and allows processed materials to float freely in solution. LAL has proven to be an efficient, environmentally friendly[58,59] method for the bottom-up and top-down synthesis of various nanoparticles.[60] LAL works by creating high-energy ionization of the solvent, leading to hydrated electrons[61] and extreme temperature and pressure capable of fracturing suspended particles while facilitating specific functionalities.[62,63] Successful BNQD synthesis has been performed with LAL in NMP,[63] EtOH, diethylamine, and ethylenediamine.[62]

Recently, Muneoka sought to investigate the effect of LAL on the size and dispersibility of h-BN in water.[61] The ionization of water molecules is capable of producing hydrated electrons[64–66] and free hydroxyl species,[67,68] both of which are important in the functionalization process. After 60 min of femtosecond laser irradiation, the average size of h-BN particles was reduced by 29% from 160 to 114 nm (Fig. 8); 30 min was enough to produce nanoparticles in the 5–10 nm size range. Dispersion stability was assessed through temporal gradient measurements of optical thickness at 500 and 800 nm wavelengths for different processing times. The result was an unexpectedly low sedimentation rate for the 60 min ablated sample compared to pristine h-BN when accounting for particle size reduction and Stokes' law. Zeta potential measurements showed a decrease from pristine h-BN to the 60 min sample, which might indicate surface modification by the hydroxyl radicals created during processing. Laser ablation in liquid has proven effective at reducing the sizes of suspended particles and inducing functionalization. Since the active synthesis region is concentrated around the laser fluence, LAL will require lengthy processing times with constant stirring to generate particle size reduction at sufficient yields. In addition to laser optimization, choosing a solvent is important due to the unavoidable creation of radical species from cooling the plasma field generated during the treatment.[61] In addition to the basic energetic methods such as ultrasonication and laser ablation, top-down synthesis of BNNSs/QDs depends on modifying the surface states through defect formation and subsequent functionalization or adjusting the bulk properties through ion intercalation or the use of highly polar solvents. These methods can produce BNNSs but are still relatively ineffective at yielding sizable amounts of highly luminescent BN QDs.

B. Bottom-up methods

Bottom-up methods can be classified on whether the synthesis method leads to epitaxial or non-epitaxial growth.[42] CVD, physical vapor deposition, pulse laser deposition, and pyrolysis are examples of epitaxial growth.[69] For brevity, this review will briefly cover the CVD techniques for epitaxial and non-epitaxial growth of h-BN nanosheets. For more information, Naclerio[70] offers an in-depth review of the mechanisms regarding CVD growth of mono- and few-layered h-BN crystals on various substrates, while Molaei[69] briefly covers other epitaxial growth procedures. Non-epitaxial growth can include unbounded[71–73] and scaffolded[74–76] CVD methods, HTP-assisted solid state[77,78] and HTP hydrothermal/solvothermal[79–83] reactions, as well as the annealing of solid precursors.[10,78,84,85]

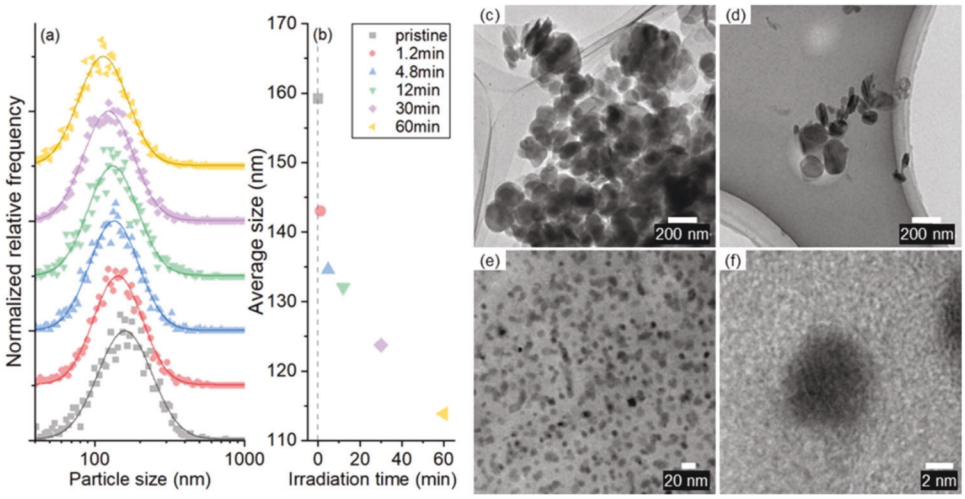

FIG. 8. Effect of irradiation time on the size of h-BN particles. (a) Particle size with counting statistics, (b) particle size as a function of irradiation time, (c) TEM of stock (untreated) BN powder, and (d)–(f) TEM of h-BN after 30 min of laser treatment. Reproduced with permission from Muneoka *et al.*, J. Phys. D: Appl. Phys. **57**, 245205 (2024). Copyright 2024 Institute of Physics.

1. Chemical vapor deposition

CVD relies on gaseous precursors such as boron and nitrogen sources to initiate particle growth through the adsorption of reacted vapors onto catalysts. This method is popular for synthesizing nanomaterials since the adjusting physical and chemical parameters (temperature, gas flow rates, precursor materials, and catalyst properties) can produce nanoparticles with various characteristics. CVD methods can include boron and nitrogen sources as separate precursors (boron trifluoride, boron trichloride, or diborane with ammonia), but high toxicity and stoichiometric balancing can make these ingredients undesirable.[42] Single compound sources such as borazine and gaseous ammonia borane (or borazane, AB) have been employed to remedy this.[35,70,86] CVD methods are susceptible to substrate morphology,[69] catalyst morphology and crystallinity,[70] substrate interaction strength,[42] and gas composition.[87] A process diagram with scanning electron microscopy (SEM) images of intermediate growth steps is shown in Fig. 9.

Epitaxial CVD relies on the nucleation of gaseous or vaporized precursors to initiate grain seeding onto a substrate. Various shapes of h-BN crystals have been grown, including diamond,[89] triangular,[90–93] and hexagonal.[94] In the past, HTP CVD (>4 GPa and >1400 °C) has been reliable for growing high-quality h-BN films, but the extremely high temperatures and pressures limit scalability.[95–98] For example, h-BN crystal growth on sapphire requires high synthesis temperatures due to its poor catalytic activity.[99–104] Epitaxial alignment was found when h-BN was grown on sapphire at >1400 °C, exhibiting zig-zag edge matching on the sapphire substrate's (1120) plane across its entire surface, two inches in diameter. Jang *et al.* attributed the larger interlayer distance in upper layers to the slight corrugation of the bottom layer (0.34 vs 0.33 nm).[104] Epitaxial catalytic CVD, which catalyzes BN crystal growth, offers a route for h-BN synthesis with lower pressure and energy requirements.[70] Due to its heteroepitaxy, the h-BN/substrate complex is sensitive to the strain caused by lattice mismatch and the differences in their coefficients of thermal expansion.[42,69,105] In addition, grain edges can limit single-crystal growth, with a study finding that h-BN coverage can substantially reduce catalyst substrate reactivity.[87] Experiments have grown h-BN crystals on copper[3] and nickel[86] substrates, obtaining lattice mismatches of 2% and 0.4%, respectively. Adjusting for higher interaction strength, such as with Ni (111),[92,106,107] Rh (111),[108] and Ge (100) and Ge (110),[109] can allow for the synthesis of larger, similarly oriented domains with seamless boundaries.

Precursor choice can drastically affect the morphology of h-BN films. Independent B and N sources may be necessary for monolayer deposition of h-BN depending on their respective consumption rates.[70] Different ratios of input gases can also favor specific morphologies; for example, a larger influx of nitrogen could lead to higher quality h-BN films and potentially inhibit boron species deposition by saturating the surface with nitrogen.[110] Solid precursors may also require pyrolysis and a carrier gas for effective vapor dissemination. Kim *et al.* suspected the carrier gas was transferring incompletely pyrolyzed precursor by-products and introducing particle impurities to the crystal growth.[89] By excluding the carrier gas, they could produce atomically flat (1.81 Å) monolayer h-BN crystals with domain sizes up to 4 μm^2 on SiO_2/Si substrate. A common concern for monolayer growth is the surface corrugation arising from different coefficients of thermal expansion,[111] a problem that could be resolved by implementing buffer layers to reduce strain.[112,113]

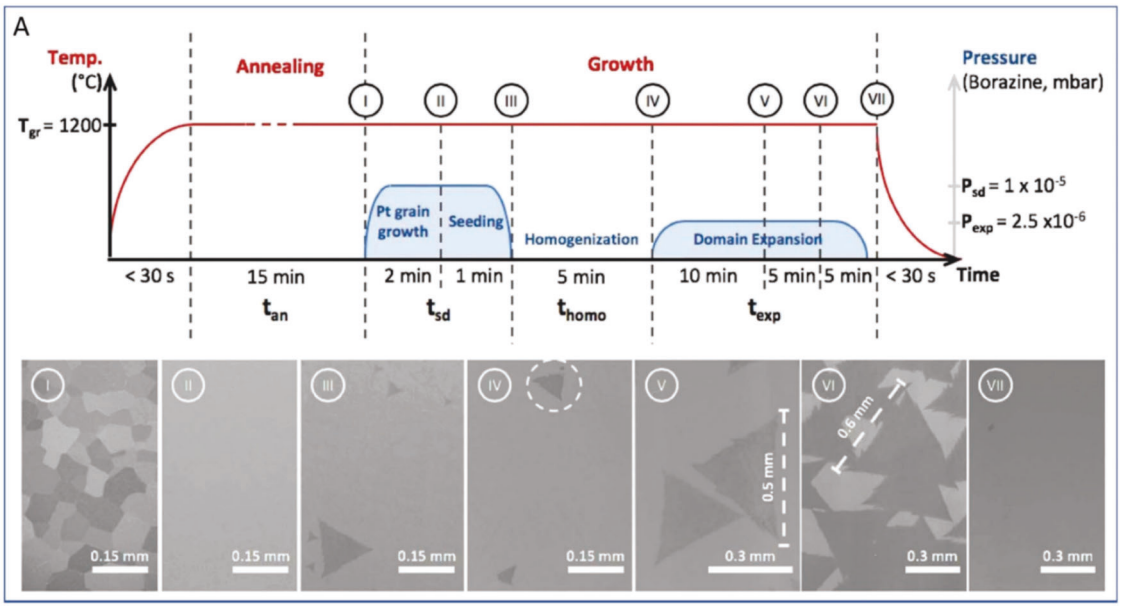

FIG. 9. (a) Growth process diagram for the epitaxial growth of h-BN on Pt substrate. (b) SEM images of the synthesis process throughout the procedure. Reproduced with permission from Wang *et al.*, ACS Nano **13**(2), 2114–2126 (2019). Copyright 2019 American Chemical Society.[88]

Allowing the sheets to grow over the grain barrier can achieve non-epitaxial CVD growth of BNNSs. The crowding causes folding up and vertical alignment of the nanosheets with thicknesses less than 4 nm, exhibiting increased crystallinity at higher synthesis temperatures.[71] The electric field formed through microwave plasma CVD can also induce vertical growth, with a morphology controllable by the ratio of precursor gases.[72,73] Unaligned BNNSs can be grown on complex surfaces to form hybrid structures, with examples including silicon nitride nanowires,[74] BN fibers,[75] and zinc sulfide nanoribbons.[76]

2. Solid state crystallization (SSC)

SSC requires the treatment of solid precursors at a high temperature to induce the crystallization of h-BN. While this method can synthesize bulk h-BN for further top-down processing,[10,50,114] the growth parameters can be controlled to synthesize BNNSs directly.[78,85,115,116] Li *et al.* synthesized BNNSs bottom-up and BN QDs top-down as less toxic luminescent QDs to investigate temperature-dependent PL mechanisms.[115] Their BNNSs were produced by dissolving diborane trioxide and urea in methanol at a ratio of 1:10, then stirring for 24 h. The precursor material was transferred to a quartz boat and annealed under an ammonia atmosphere at various temperatures. h-BN crystallization, although poor, was found to have occurred at 600 °C, evidenced by a broad XRD peak at 24°–26° that was reasonably invariant between the samples. Better evidence of h-BN quality may come from the FTIR data, showing the B_2O_3 peaks mostly disappearing above 700 °C, with minor B–O signals at 1099 and 652 cm^{-1} indicating some amount of functionalization with leftover oxygen species. Visible sheets were present under SEM at 900 °C with lateral sizes up to several micrometers. Their thickness was determined to be 4–8 layers through HRTEM with an interlayer distance of 0.34 nm, reconfirmed by AFM showing thicknesses between 1.8 and 2.7 nm. These as-synthesized BNNSs show no PL response until after sonication, where they exhibited blue light emission (365 nm) and a QY of 15.4%, assumedly due to few-layered h-BN's penchant to collect defects when paired with highly polar solvents, leading to the surface state mediated PL emissions.[55]

In addition to its use as a sublimated precursor for epitaxial growth of h-BN films,[3] AB has also been used to prepare few-layer BNNSs in molten salt solutions for its lack of carbon and convenient polymerization pathway.[78,117] Similarly, various groups[116,118,119] have used molten salt solutions with several combinations of independent boron and nitrogen sources, but these precursors would often be responsible for an abundance of carbon impurities.[120,121] Molten salt media can stabilize bond formation due to ion polarization,[122,123] with the liquid phase conveniently reducing the nucleation energy barrier.[124] In 2021, Liu synthesized BNNSs by mixing AB with potassium chloride and sodium chloride before annealing at 1000 °C.[85] The resulting product exhibited lateral dimensions up to 4 μm, with the higher ratios of salt to AB producing larger and thinner BNNSs. AFM showed that BNNSs from the highest salt concentration were 0.5–4 nm thick. They attributed the slightly larger lattice spacing (0.34 vs 0.33 nm) to poor crystallization during the extremely short dwell time of two minutes, finding that longer dwell times led to thicker BNNSs. XPS shows dominant B–N bonding in the B 1s and N 1s peaks, while FTIR shows clean spectra with prominent B–N stretching and bending peaks at 1371 and 798 cm^{-1}, respectively, and broad N–H absorption at lower synthesis temperatures. Any hydroxyl functionalization was suspected to have occurred during the washing procedure.

3. Hydrothermal/solvothermal

Bottom-up production of BN QDs usually involves the synthesis of h-BN materials that are subjected to top-down processes. In contrast, true bottom-up production methods for BN QDs typically involve a HTP catalyzed reaction between dissolved precursors.[51,125] Bottom-up production is more easily scalable[42,126] and tunable than traditional top-down methods. Still, it normally exhibits low purity due to the ubiquity of organic and oxygenous precursors such as boric acid, urea, and melamine.[44,82,83,127] Gram-scale production was achieved using zinc, magnesium, and iron particles to catalyze the growth of polycrystalline BNNSs in HTP conditions with B_2O_3 and hydrazine as precursors, showing varying morphology and yield based on the chosen catalyst.[126] Specific choice of precursors can enable nanoparticle morphologies and functionalities customization, which is helpful given the surface-state mediated PL response.[55] Huo's group chose boric acid and melamine as precursors for HTP hydrothermal synthesis of BN QDs with blue fluorescence.[127] After finding B–O and N–H bonds through XPS analysis, they deemed the experiment successful. Similarly, Xue reported higher PL emissions from the increased amination in BCNOQDs vs BN QDs after hydrothermal treatment.[128] Precursor choice has been studied extensively to find affordable, environmentally friendly, and less toxic sources of boron and nitrogen.[44] For example, Kong synthesized BN QDs in a single step through the hydrothermal treatment of boric acid and tryptophan.[79] They tested a variety of amino acids due to their nitrogen content, biocompatibility, and affordability. TEM and HRTEM showed a spherical morphology with an average diameter of 3.05 nm, with FTIR peaks at 1628, 1460, and 1068 cm^{-1} being attributed to B=N, B–N, and N–B–O, respectively. Consoli produced carbon-doped BN QDs through HTP solvothermal treatment of urea and 4-hydroxyphenyl boronic acid dissolved in DMF.[82] Their goal was to synthesize BN QDs with superior water dispersibility and biochemical applications arising from phenolic and carboxylic functionalities, comparing the same synthesis method to a combination of boric acid and urea. Other common precursors include ammonia solution and ammonium hydroxide.[80,81]

Of the three bottom-up methods included, only hydrothermal/solvothermal methods can directly produce luminescent BN QDs, but they are prone to heavy contamination from precursor, additive, and solvent choices—analogous to similar top-down techniques. Alternatively, epitaxial CVD can produce highly ordered, monolayer BNNSs for non-biological applications, while non-epitaxial CVD and SSC methods can produce much higher yields of BNNSs that must be subjected to potentially cumbersome extraction procedures before further top-down treatments for the synthesis of BN QDs.

C. Summary of the synthesis methods

We summarized the top-down synthesis methods in Table I to enhance productive readership and provide further reading. Here, SALE stands for sonication-assisted liquid exfoliation. As summarized, most of the products from the top-down synthesis methods are small in lateral dimension, i.e., leading to BN QDs, with some

TABLE I. Top-down synthesis methods.

Year	Product	Method	Solvent	Additive/precursors	Height	Size	QY%	Emission	References.
2015	BNNS	SALE	DMF	···	···	···	···	···	38
	BNQD	HTP solvothermal	DMF	···	0.85–2.17 nm	3.19 nm	19.50%	···	38
2016	BNNS	HTP hydrothermal	H_2O	NaOH, KOH	···	···	···	···	128
	BNQD	HTP hydrothermal	H_2O	KOH	1.05 nm	3.3 nm	1.80%	410 nm	128
2016	BNQD	SALE with ion intercalation	H_2O	H_3PO_3	3.5 nm	3–6 nm	···	···	41
2014	BNNS	SALE	H_2O, IPA, MEG	···	<1 nm	···	···	···	10
	BNQD	Reflux solvothermal	MEG	···	···	<6 nm	···	413 nm	10
2022	BNQD	HTP solvothermal	EtOH	PPD	···	4.9 nm	···	···	57
2019	BNNS	Ion intercalation and HTP solvothermal	EtOH	NaOH	1 nm (monolayer)	0.3–4.6 μm	···	···	39
	BNQD	Ion intercalation and HTP solvothermal	EtOH	NaOH	0.8 nm	5.1 nm	···	435 nm	39
2014	BNQD	Ion intercalation	$EtOH/H_2O$	KOH	0.9 nm	10 nm	2.50%	425 nm	14
2018	BNNS	HTP hydrothermal ion intercalation then SALE	N_2H4/H_2O then $EtOH/H_2O$	···	···	···	···	···	45
	BNQD	HTP hydrothermal ion intercalation	H_2O	KOH	0.86–1.18 nm	1.0–2.6 nm	4.16%	395 nm	45
2021	BNQD	Laser ablation	EDA	···	Few-layer	1.6 nm	18.40%	480 nm	62
	BNQD	Laser ablation	DEA	···	Few-layer	1.8 nm	22.80%	480 nm	62
	BNQD	Laser ablation	EtOH	···	Few-layer	1.4 nm	3.80%	480 nm	62
2019	BNQD	Laser ablation and SALE	NMP	···	1 nm	2.1 nm	···	460 nm	63
2021	BNNS	SALE	H_2O/EtOH/Ace	···	···	···	···	···	40
2015	BNQD	SALE and reflux solvothermal	DMF, DMSO	···	2.5 nm	3.3 nm	8.60%	442 nm	54
2017	BNQD	SALE then HTP solvothermal	NMP	···	1.3 nm	2.0 nm	21.30%	505 nm	52
	BNQD	SALE then HTP solvothermal	DMF	···	2.6 nm	2.8 nm	16.40%	445 nm	52
	BNQD	SALE then HTP solvothermal	EtOH	···	4.0 nm	4.1 nm	12.60%	420 nm	52
2021	BNNS	Modified Hummers' method	H_2O	H_2SO_4, $KMnO_4$	1.78 nm	486 nm	···	···	50
2020	BNQD	HTP hydrothermal	DMF	···	1.8–2.7 nm	4.6 nm	···	474 nm	115
2023	BNNS	Ion intercalation and HTP hydrothermal	H_2O	NaOH, LiCl	1–2.9 nm	1.18 μm	···	···	49
2021	BNQD	SALE and HTP solvothermal	NMP	$CO(NH_2)_2$	···	14 nm	32.27%	420 nm	55
	BNQD	SALE and HTP solvothermal	H_2SO_4/H_2O	PPD	···	···	11.87%	510 nm	55
	BNQD	SALE and HTP solvothermal	Ace	$SC(NH_2)_2$	···	5.5 nm	8.50%	528 nm	55
	BNQD	SALE and HTP solvothermal	DMF	PPD	···	···	22.50%	575 nm	55
	BNQD	SALE and HTP solvothermal	EtOH	PPD	···	2.5 nm	19.79%	610 nm	55
2022	BNQD	SALE and HTP solvothermal	EtOH	PPD	···	4.9 nm	···	461 nm	57
2022	BNNS	SALE and ion intercalation	H_2O	NaOH	···	···	···	···	47
2024	BNNP	Laser ablation	H_2O	···	···	5–10 nm	···	···	61
2015	BNNS	Dry ball milling	···	$CO(NH_2)_2$	2.5 nm	100 nm	···	···	56
2014	BNNS	Wet ball milling then SALE	NMP	···	Few-layer	<300 nm	···	···	24
2016	BNNS	Wet ball milling	H_2O	NaOCl	50–200 nm	100–1000 nm	···	···	27
2011	BNNS	Ball milling then SALE	···	$C_{14}H_{12}O_2$	<4 nm, <10 layers	250 nm	···	···	25
2012	BNNS	Wet ball milling then SALE	H_2O	···	1.2–8 nm	10–500 nm	···	···	26
2019	BNNS	Dry ball milling	···	H_3BO_3	2 nm	2 μm	···	···	28
2019	BNNS	Dry ball milling	···	Sucrose	4.4 nm	98 nm	···	···	28

success of BNNSs. Similarly, we summarized the bottom-up synthesis methods in Table II. In contrast, the bottom-up approaches are preferential to produce BNNSs, although some attempts were reported for BN QDs.

In addition, we also summarized the CVD synthesis method of h-BN crystals (including BNNSs and thicker products) in Table III. CVD is a popular method for many nanomaterials, including graphene, TMDs, etc. CVD synthesis of h-BN relies on specific substrates such as metals (Cu, Ni, etc.) with B and N growth species solubility or dielectric crystals (Ge and Sapphire) that offer close lattice matching with h-BN.

IV. BIOMEDICAL APPLICATIONS OF BNNSs, BN QDs, AND BN DOTS

h-BN is known for its high chemical stability due to its covalent sp^2 B–N bonds,[129] making it resilient even in wet conditions.[42] Maintaining balanced boron intake is essential, as boron plays a role in various physiological processes and is linked to certain diseases, including melanosis, bone growth issues, and cancer.[130] Since h-BN is inherently hydrophobic, surface functionalization is needed before using BN nanostructures for biomedical applications.[131,132] BNNSs are also being explored for gene delivery, where their structural characteristics may enhance cellular uptake and protect genetic material during transport,[133] and potential in cancer therapy.[134] In Subsections IV A–IV G, we will discuss some examples of drug delivery, imaging, tissue engineering, therapeutics, and antibacterial and antiviral applications.

A. Drug delivery

1. Doxorubicin delivery

Doxorubicin (DOX) is widely used in clinical chemotherapy to induce tumor cell apoptosis by inhibiting DNA replication. It achieves this through oxidative DNA damage and targeting topoisomerase II (TOP II). As a cell cycle non-specific drug, DOX effectively inhibits tumor cells across various stages of growth. To enhance DOX's therapeutic efficacy while minimizing its toxicity, a range of boron nitride (BN) nanocarriers have been designed and studied to improve delivery and reduce side effects.[135] Weng *et al.* successfully synthesized a highly hydroxylated boron nitride [$BN(OH)_x$] nanocarrier using a "reserved reaction" approach, effectively addressing the inherent chemical inertness of h-BN.[136] $BN(OH)_x$ was fabricated by thermally substituting C atoms with boric acid substructures in graphitic carbon nitrides [Fig. 10(a)]. This hydroxylated BN was water-soluble and biocompatible, achieving an impressive DOX-loading capacity of up to 300%, which proved more effective than free DOX in reducing cancer cell viability.[135,136]

$BN(OH)_x$ exhibited a porous structure in white BN powder form and can form aqueous suspensions at a 2.0 mg/ml concentration [Fig. 10(b)]. The authors attributed the high drug-loading capacity to the lightweight nature of BN and π–π interactions between DOX molecules and the conjugated BN domains. The DOX-loaded BN demonstrated a controlled release profile, with slow release in neutral conditions and rapid release under acidic conditions [Figs. 10(c) and 10(d)]. Cytotoxicity testing revealed minimal toxicity for the hydroxylated BN alone over 24 h, even at concentrations of 100 μg/ml [Fig. 10(e)]. However, the DOX-loaded BN exhibited significantly higher cytotoxicity than free DOX. For instance, after 24 h at a concentration of 2.0 μg/ml, free DOX reduced cell viability to 38%, while the same dose of DOX-loaded $BN(OH)_x$ reduced viability further to 18%–21% [Fig. 10(f)]. This enhanced efficacy was likely due to the greater cellular uptake of DOX@$BN(OH)_x$ through endocytosis compared to the passive diffusion of free DOX across cell membranes. Once internalized, the acidic environment of the lysosome (pH ~ 5.5) triggered the release of DOX, thus facilitating targeted delivery within cancer cells.[135]

2. Camptothecin delivery

Camptothecin (CPT) has anti-cancer effects by targeting DNA topoisomerase I (TOPO I). By blocking the re-joining step of TOPO I's cleavage reaction, CPT causes the accumulation of intermediate complexes, disrupting DNA replication in cancer cells. However, CPT's poor solubility in water necessitates frequent low-dose administration to achieve therapeutic efficacy. This limitation highlights the need for drug delivery systems to stabilize CPT and enhance its solubility.

Cheng *et al.* explored hydroxylated boron nitride nanosheets (OH-BNNSs) as effective CPT carriers to address these challenges.[137] These BNNSs, synthesized using a scalable NaCl template method, were hydroxylated with nitric acid to improve dispersion and stability. TEM analysis revealed that the BNNSs produced at 900 °C featured sheet-like structures with lateral sizes between 40–120 nm and 2.0–4.0 nm thicknesses. CPT, being hydrophobic, absorbs onto OH-BNNS surfaces via hydrophobic interactions, achieving a drug-loading capacity of up to 170 wt. %. Notably, due to their chemically inert nature, the BNNSs retained significant hydrophobic regions even after hydroxylation.

In vitro studies demonstrated that OH-BNNSs showed minimal cytotoxicity at concentrations as high as 100 μg/ml, maintaining 99% cell viability. Free CPT at 1.0 μg/ml reduced cell viability to 76% after 24 h, which decreased to 48% when CPT was loaded into OH-BNNSs. After 48 h, cell viability further dropped to 17%. *In vivo*, OH-BNNSs loaded with CPT inhibited tumor growth by 43% after 14 days of treatment, underscoring their potential as a robust drug delivery system (Fig. 11).

B. Gene delivery

DNA, RNA, and proteins are vital biomolecules with significant roles in modern medicine and advanced biomedical technologies, such as gene therapy, RNA vaccines, and diabetes management. Despite their therapeutic potential, these biomolecules often have high molecular weights and are inherently unstable within the body. Consequently, developing effective carriers is essential to enhance their stability and fully harness their therapeutic capabilities.[138]

BNNSs were used to deliver two sets of hairpin G-quadruplex (HG1 and HG2) DNAs and copper (II) phthalocyanine (Cu-Pc), as shown in Figs. 12(a) and 12(b), forming nanohybrids capable of accumulating in tumor sites.[139] In these systems, Cu-Pc is a photosensitizer for photodynamic therapy (PDT) while enabling *in situ* detection and visualization of miR-21 using surface-enhanced Raman spectroscopy (SERS). As shown in Fig. 12(c), HG1 was employed to hybridize with miR-21. It produced a single-stranded tail in HG1, which dissociated and increased the mobility of HG1

TABLE II. Bottom-up synthesis methods.

Year	Product	Method	Solvent/Substrate	Additive/precursors	Height	Size	Emission	References
2017	BNQD	HTP hydrothermal	H_2O	H_3BO_3, $C_3H_6N_6$	0.7 nm	3 nm	400 nm	127
2021	BNQD	HTP hydrothermal	H_2O	H_3BO_3, $C_3H_6N_6$	⋯	⋯	⋯	83
2020	BNNS	SSC	MeOH	B_2O_3, $CO(NH_2)_2$	Few layer	>1 μm	⋯	115
2020	BNQD	HTP hydrothermal	H_2O	H_3BO_3, Trp	⋯	3.05 nm	Blue	79
2022	BNQD	HTP hydrothermal	H_2O	H_3BO_3, NH_4OH	2–5 nm	⋯	⋯	81
2021	BNNS	SSC	Molten KCl–NaCl	AB	Few layer	<4 μm	⋯	85
2010	BNNS	SSC	⋯	H_3BO_3, $CO(NH_2)_2$	0.5–0.9 nm	<1 μm	⋯	114
2024	CBNQD	HTP solvothermal	DMF	4-HPBA, $CO(NH_2)_2$	⋯	1.8 nm (excitation dependent)	480 nm	82
	BNQD	HTP solvothermal	DMF	H_3BO_3, $CO(NH_2)_2$	⋯	⋯	⋯	82
2023	BNQD	HTP hydrothermal	H_2O	H_3BO_3, NH_3 (aq)	⋯	3–5 nm	⋯	80
2021	BNNS	Pyrolysis and homogeneous crystallization	⋯	AB, N_2	3 nm, 8 layers	30 nm	⋯	84
	BNNS	Pyrolysis and heterogeneous crystallization	⋯	B, N_2	7–8 nm, 20 layers	100 nm	⋯	84
2011	BNNS	SSC	⋯	AB	1–5 nm, 1–7 layers	100 μm	⋯	78
2011	BNNS	SSC	Molten LiCl–KCl	$NaBH_4$, $CO(NH_2)_2$	<10 nm	⋯	528 nm	116
2011	BNNS	Non-epitaxial CVD	Si/SiO_2	B/MgO/FeO, NH_3	<5 nm	⋯	⋯	71
2018	BNQD	HTP hydrothermal	H_2O	H_3BO_3, NH_3	0.91 nm	1.71 nm	410 nm	53
2011	BNNS	Microwave plasma CVD	Si	BF_3, N_2, H_2	<10 layers	<2.5 μm	⋯	73
2011	BNNS	Surface-mediated HTP solvothermal	Zn powder	B_2O3, Cl_2H_4N	4 nm	226 m^2/g	⋯	126
2019	BNNS	SSC then SALE	Molten NaCl–KCl then EtOH	Borax, $C_3H_6N_6$	1 nm, 3 layers	50 nm	⋯	119
2011	BNNS	SSC then SALE	H_2O then DMF, DMSO, or EDC	$NaBF_4$, NaN_3, NH_4Cl	2–5 nm	10 nm	⋯	77
2011	BNNS	Non-epitaxial CVD	ZnS nanofibers	B, B_2O_3, Fe_2O_3, NH_3	Few layer	⋯	⋯	75
2006	BNNS	Non-epitaxial CVD	Si_3N_4 nanowires	H_3BO_3, $C_3H_6N_6$, N_2, B_2O_3, NH_3	⋯	⋯	⋯	74
2010	BNNS	CVD	Copper	AB	2–5 layers	>1 μm	⋯	6
2020	BCNNS	SSC	Molten NaCl–KCl	B_2O_3, $C_3H_6N_6$, $C_6H_{12}O_6$	0.4 nm	10 μm	⋯	122

TABLE III. Epitaxial CVD growth of h-BN crystals.

Year	Substrate	Precursors	Height	Size	References
2014	Copper	AB	Monolayer	35 μm^2	93
2015	Germanium	AB	Monolayer	1 μm^2	109
2011	Rhodium	$B_3N_3H_6$	Monolayer	1 cm^2 (coalesced)	87
2011	Nickel	$B_{10}H_{14}$, NH_3, N_2	2 nm	>100 μm	107
	Copper	$B_{10}H_{14}$, NH_3, N_2	2–15 nm	>100 μm	107
2003	Nickel	$B_3N_3H_6$	Monolayer	⋯	106
2016	Sapphire	TEB, NH_3	1.5 nm, 5 layers	⋯	112
2018	Sapphire	TEB, NH_3	<4 layers	⋯	118
2011	Sapphire	TEB, NH_3	400 nm	⋯	113
2010	Rhodium	$B_3N_3H_6$	Monolayer	⋯	108
2014	Copper	AB	0.59 nm	⋯	90
2010	Nickel	$B_3N_3H_6$	5–50 nm	<20 μm	86
2012	Copper	AB	0.42 nm	⋯	89
2016	Sapphire	AB	2–6 layers	2 in (whole wafer)	104
2016	Sapphire	TEB, NH_3	30 nm	2 in (whole wafer)	105

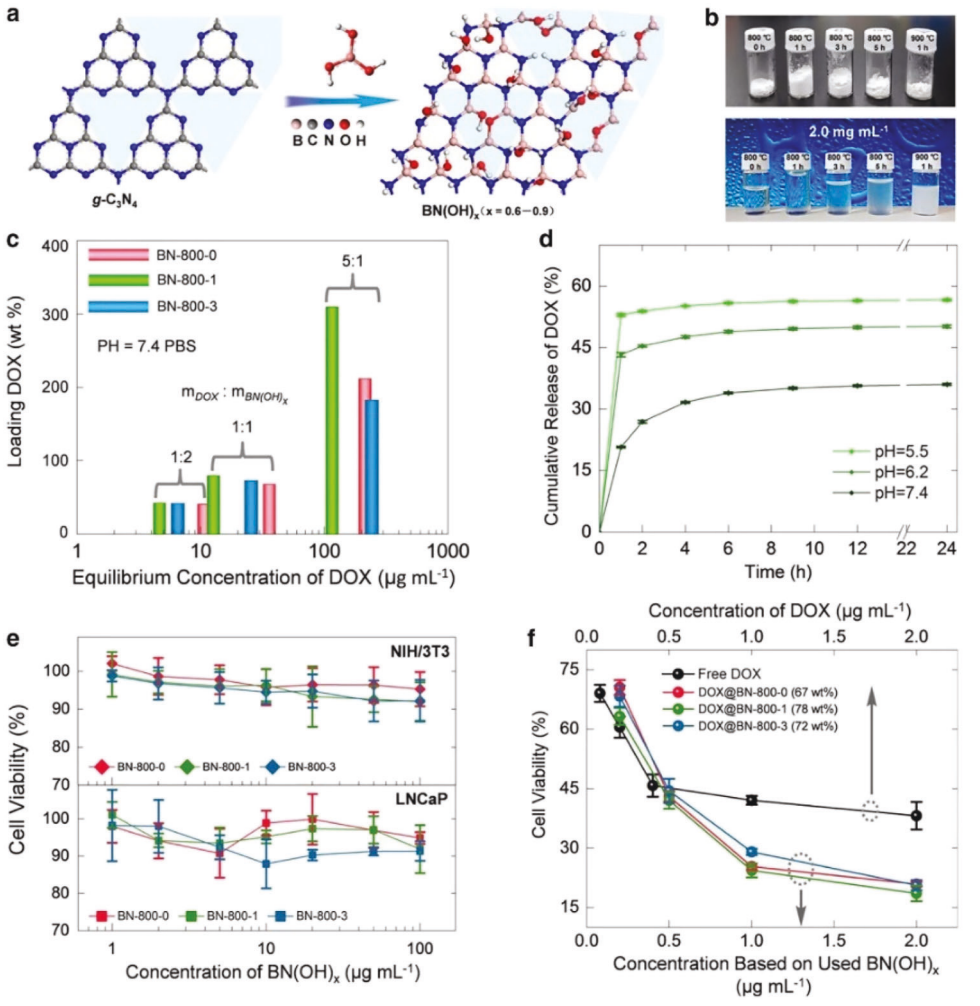

FIG. 10. (a) Illustrates the "reserved reaction" for forming hydroxylated BN powders. (b) Photographs of the as-prepared powders and the corresponding aqueous solutions/suspensions. (c) DOX loading capacities on the hydroxylated BN at different equilibrium conditions. (d) Release kinetics of DOX in different pH buffers. (e) Cell viability of NIH/3T3 mouse embryonic fibroblast cells and LNCaP human prostate cancerous cells incubated with hydroxylated BN solutions at different concentrations for 24 h. (f) Cell viability of LNCaP cells after incubation with DOX@BN(OH)$_x$ and free DOX solutions for 24 h. Reproduced with permission Wang *et al.*, BMEMat **2**, e12068 (2024). 2024 Author(s), licensed under a Creative Commons Attribution 4.0 License.

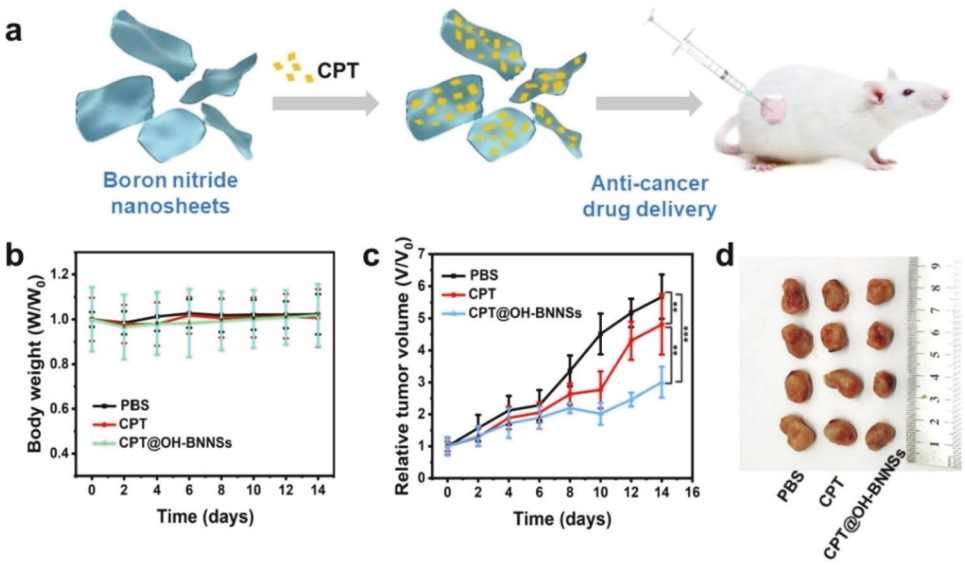

FIG. 11. (a) Schematic illustration of the *in vivo* experiments with CPT@OH-BNNSs. (b) Body weights of different groups of mice by different treatments. (c) Tumor growth curves and (d) photographs of tumors exfoliated from each group after the sacrifice of mice. Reproduced with permission from Cheng *et al.*, Chem. Eng. J. **437**, 135304 (2022). Copyright 2022 Elsevier Science.

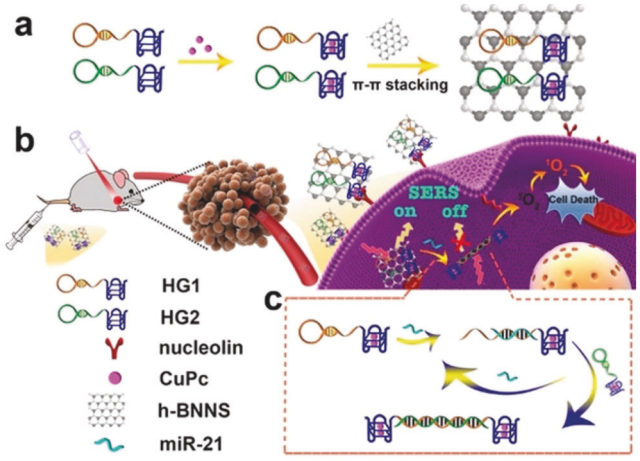

FIG. 12. Schematic illustration of (a) the synthesis of CuPc@HG@BN, (b) the antitumor and SERS monitoring mechanism, and (c) the amplification of miR-21 in living cells. Reproduced with permission from J. Liu, T. Zheng, and Y. Tian, Angew. Chem., Int. Ed. **58**(23), 7757–7761 (2019). Copyright 2019 Wiley-VCH Verlag GmbH & Co. KGaA.

on h-BNNS, facilitating its hybridization with HG2. The exfoliated BNNSs, with a uniform size of ~90 ± 10 nm, serve as SERS substrates, offering high enhancement factors (EFs) and excellent uniformity due to interfacial dipole interactions between Cu-Pc and the polar B–N bonds.

These CuPc@HG@BN nanohybrids are stable in physiological conditions and capable of real-time imaging and miR-21 monitoring. Furthermore, the Cu-Pc component generates singlet oxygen ($^1O_2$) during PDT, causing significant cellular damage within 8 h. Stability studies demonstrated that Cy3-labeled CuPc@HG@BN accumulates in tumor tissues and remains intact for at least 48 h. In therapeutic evaluations, early stage tumors were eradicated after three days of treatment with 25 μg/ml of CuPc@HG@BN. However, for advanced-stage tumors, complete elimination was not achieved even with 200 μg/ml of the nanohybrid after 15 days of treatment, underscoring the challenges of treating late-stage malignancies.

C. Bioimaging

Boron nitride nanosheets (BNNSs) have intrinsic fluorescence due to structural defects within their lattice, such as vacancies and edge states.[140] In monolayer (ML) BNNSs, a direct-gap emission around 6.1 eV (194 nm) was detected. The emission from few-layer (FL) BNNSs is less intense, due to the indirect gap transitions of 5.71–5.95 eV (208–217 nm). BNNSs with stacking faults will move the emission to longer wavelengths (~220–230 nm). By adjusting factors such as size, adding dopants, and modifying the surface, BN nanomaterials may achieve impressive luminescent properties in the UV-visible range, making them ideal for use in bioimaging.

One of the key strengths of BNNSs is their chemical stability. They are highly resistant to degradation under biological conditions, ensuring their fluorescence properties remain consistent throughout imaging experiments. This makes them more reliable than conventional dyes, which are prone to degradation or photobleaching over time.[141] In addition to their intrinsic properties, BNNSs can be functionalized with biomolecules, such as antibodies, peptides, or DNA, through surface chemistry techniques. By attaching functional groups to the BNNS surface, these nanosheets can be tailored to bind specifically to target biomolecules or cellular receptors. This capability enables precise imaging of particular cells, tissues, or biological structures. The non-toxic composition of BNNSs, made of boron and nitrogen, makes them safer than quantum dots that often contain heavy metals such as cadmium (CdS and CdSe), which pose biological and environmental risks. Cytotoxicity studies confirm that BNNSs exhibit minimal toxicity, making them suitable for live-cell imaging applications.[142]

Lin *et al.* reported the synthesis of BN QDs by ultrasonic treatment of potassium intercalated h-BN.[9] The author detected excitation-dependent fluorescence in the visible range, as described in Fig. 3 earlier. These emissions are attributed to three types of luminescent centers: carbon-replaced N vacancies, a carbene structure at the zig-zag BN edges, and BO_x species. The authors found that BN QDs are biocompatible with the mammalian cell line, MDCKII, at low doses (0–40 μg/ml). Luminescent cell imaging was also reported, as performed using confocal microscopy in the FITC (fluorescein isothiocyanate) mode of MDCKII cells after 24h incubation. Figure 13(a) shows the microscopy images of the cells stained with BN QDs alone. The QDs were internalized into cells but did not penetrate the cell nuclei. Figure 13(b) shows the MDCKII nucleus stained with DAPI (4′,6-diamidino-2-phenylindole, emission from around 400–650 nm). Figure 13(c) shows BN QDs in the FITC green channel (BN QDs emit a broad fluorescence of ~325–625 nm in this case). Figure 13(d) shows the overlay image. Lin *et al.* think that although the nucleus in Fig. 13(c) also gives green emission from the nuclei, BN QDs did not penetrate the nuclear membranes, as the boundary between cells, nuclei, and cytoplasm is clear. All these results indicate that BN QDs can be used in high-contrast bioimaging and will be well-suited for other biomedical applications. The good stability, biocompatibility, and environmentally friendly nature position BN QDs as a promising alternative for advanced bioimaging applications.[54,143]

D. Bone tissue engineering

BNNSs offer high elastic modulus, large specific surface area, and high thermal stability.[144–147] These properties make BNNSs ideal for enhancing the mechanical strength of composites. BNNSs are also biocompatible with human cells.[142] Shuai *et al.* cultured the MG63 human osteosarcoma cell line and bone marrow mesenchymal stem cells (BMSCs) on Akermanite (AKM) scaffolds reinforced with BNNSs.[148] These scaffolds were fabricated and tested for improved mechanical and biological properties. At 1.0 wt. % BNNS content, the scaffolds exhibited optimal compressive strength (12.13 MPa, a 105% increase over pure AKM ceramics) and fracture toughness (2.25 MPa $m^{1}/^{2}$). These improvements were attributed to the BNNSs' ability to enhance load transfer, resist crack propagation, and dissipate energy through sheet pull-out and grain wrapping. In another study, highly compressive, cross-linker-free 3D sponges were fabricated using reduced graphene oxide (rGO) and boron nitride (BN) nanosheets via freeze-drying and thermal annealing.[149]

Another study developed 3D-printed scaffolds for bone tissue engineering using polylactic acid (PLA) reinforced with exfoliated boron nitride (EBN) (Fig. 14).[150] Physicochemical analysis confirmed EBN incorporation, while differential scanning calorimetry (DSC) and thermogravimetric analysis (TGA) indicated reduced crystallinity without affecting transition temperature. The scaffolds exhibited a mean pore size of 500 μm and maintained mechanical strength, although surface roughness increased with EBN, resulting in a hydrophilic surface. Biocompatibility tests using MG-63 and MC3T3 cells demonstrated that the scaffolds were non-toxic, suggesting potential suitability for tissue engineering applications.

Liu *et al.* discussed the challenges of functionalizing BNNSs due to chemical inertness and a low degree of covalent functionalization. They discuss different types of defects, giving mechanistic insights into tunable surface functionalization. Tailoring the surface chemistry and nanostructure of BNNSs influences their functional performance in terms of catalytic efficiency, biocompatibility, and mechanical strength in composite materials.[151] In a study, nanocomposite scaffolds with varying BN nano-powder contents were produced using freeze-drying. Collagen extracted from rainbow trout

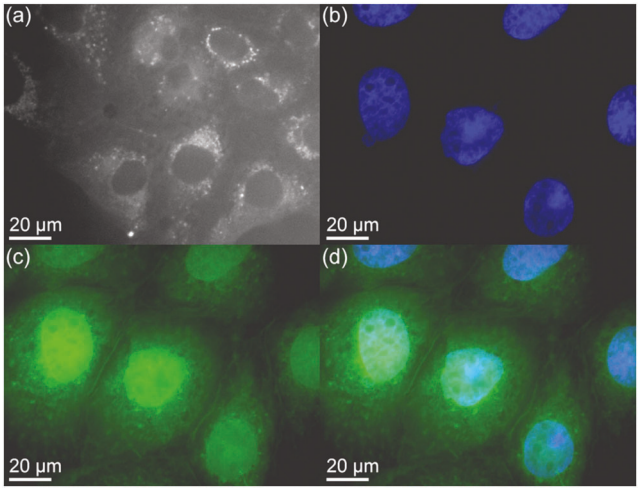

FIG. 13. (a) Confocal microscopy images of the cell, (b) images of the DAPI stained nucleus, (c) green luminescence of BN QDs surrounding the nucleus, and (d) the overlay. Reproduced with permission from Lin *et al.*, Small **10**(1), 60–65 (2014). Copyright 2013 Wiley-VCH Verlag GmbH & Co. KGaA.

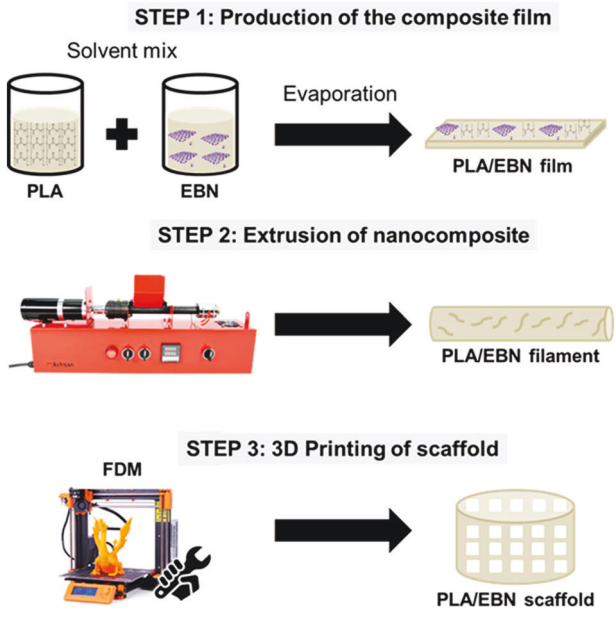

FIG. 14. Schematic of a 3D printing approach to produce bio-mimic biodegradable scaffolds made of polylactic acid (PLA). Reproduced with permission from Belaid *et al.* ACS Appl. Bio Mater. **3**(4), 1865–1874 (2020). Copyright 2020, American Chemical Society.

skin was investigated for developing collagen-BN nanocomposite scaffolds. Incorporating 6 wt. % significantly improved the scaffold's mechanical properties, which increased compressive strength and elastic modulus, making the scaffolds elastic and strong.[152]

The development of biomimetic borate-based bioactive glass scaffolds containing h-BN nanoparticles (0.1–2 wt. %) for bone tissue engineering was also explored. The scaffolds were fabricated using a polymer foam replication technique and heat treatment to sinter the structure. The characterization revealed that h-BN improved the scaffolds' compressive strength and hydroxyapatite-forming ability, enhancing their suitability for bone tissue repair. Drug release experiments showed a burst release for gentamicin sulfate due to rapid glass degradation, while 5-fluorouracil exhibited sustained release behavior, fitting the Higuchi model, and showed improved mechanical properties, bioactivity, and drug release profiles, making them promising candidates for bone regeneration and controlled drug delivery.[153] The best results were obtained by synthesizing BNNSs with tip sonication combined with Pluronic F127 acid. This produced few-layered nanosheets with a narrow size distribution and enhanced stability in water, which improved water dispersibility and biocompatibility.[142]

Alternative synthesis methods lead to new and improved properties of boron nitride nanosheets. For example, the dual functionalization approach synthesized biocompatible amphiphilic triblock copolymer Pluronic F-127 (PLU)-functionalized BNNSs (PLUBN) attributed to the synergistic interaction between the C–O dipoles and the polar B–N bonds. The hydrogen bonding between the poly(L-lactic acid) nanofiber (PLF) matrix and the PLUBN filler enhances the mechanical strength of the composite.[154] As a result of these mechanisms, the composite scaffolds show superior biological performance, such as improved adhesion, proliferation, and osteogenic differentiation of MC3T3-E1 cells, which can be helpful for piezoelectricity-driven tissue regeneration.

Due to their chemical inertness, nonmetal nitride nanomaterials such as h-BN are promising for biomedical applications. h-BN can enhance scaffold strength by supporting uniform stress distribution and crack deflection. In composites, BNNSs act as stress transfer agents, improving mechanical properties. The lubricating properties of h-BN can reduce wear on HA implants, and it has antibacterial effects when combined with HA.[155] Readers should refer to a recent review article for more bone tissue engineering of 2D materials.[155]

E. Multimodal therapeutics

BNNSs were studied for their potential use in therapeutic applications due to their high thermal conductivity, chemical stability, and biocompatibility.[156,157] Non-toxic BNNSs and their capacity to be functionalized with biomolecules further enhance their versatility in multimodal therapeutic approaches, suggesting a broad range of future biomedical applications. Zhang *et al.* synthesized hydroxy BNNSs and Pd nanohybrids (Pd@OH-BNNS) by a one-pot reduction method. Pd@OH-BNNS exhibited excellent stability and near-infrared (NIR) absorption, making it ideal for photothermal therapy (PTT) and drug delivery. With a 32% chemotherapeutic drug (DOX) loading capacity, the system enabled pH- and glutathione (GSH)-dependent, NIR-enhanced drug release, as illustrated in Fig. 15. Cellular uptake and in vitro studies showed that combining chemotherapy with photothermal treatment provided superior tumoricidal effects.[158]

Another study demonstrated BNNSs adsorbed with tannic acid–Fe complex (TA–Fe/BNNSs) absorb light in the 400–900 nm range with a photothermal conversion efficiency of 44.6%. *In vitro* tests confirmed cellular uptake in KB cells, while in vivo experiments showed significant photothermal antitumor effects, with tumor ablation upon NIR irradiation. Mice treated with TA–Fe/BNNSs showed 100% survival at doses up to 60 mg/kg, indicating a high safety profile compared to GO nanosheets. These dual-functional nanomaterials hold promise for MRI-guided phototherapy.[159]

BNNSs were evaluated for tumor treatment by boron neutron capture therapy (BNCT). BNCT is based on the emission of alpha particles from the non-radioactive boron-10 atoms upon low-energy thermal neutron beam irradiation. The alpha particles will decay after a 5–10 mm path length and damage the tumor tissues without affecting the normal cells. Therefore, BNCT potentially has fewer side effects than conventional cancer therapy. Li *et al.* combined BNCT with chemotherapy using BNNS as the carrier of DOX.[160] As illustrated in Fig. 16, ^{10}B-rich boric acid and melamine were used to prepare BNNSs by the sol-gel pyrolysis method. These BNNSs were non-covalently functionalized with DSPE-PEG-NH_2 polymer linkers for stable dispersity. DOX molecules were absorbed on these hydrophilic BNNSs to form DOX@^{10}BNNSs. Results suggest a remarkable tumor growth inhibition (TGI) of ~94.6% with combined radiochemotherapy with DOX@^{10}BNNSs and neuron irradiation, significantly outperforming the treatment only with BNNSs and neutron irradiation (TGI ~ 64.1%).

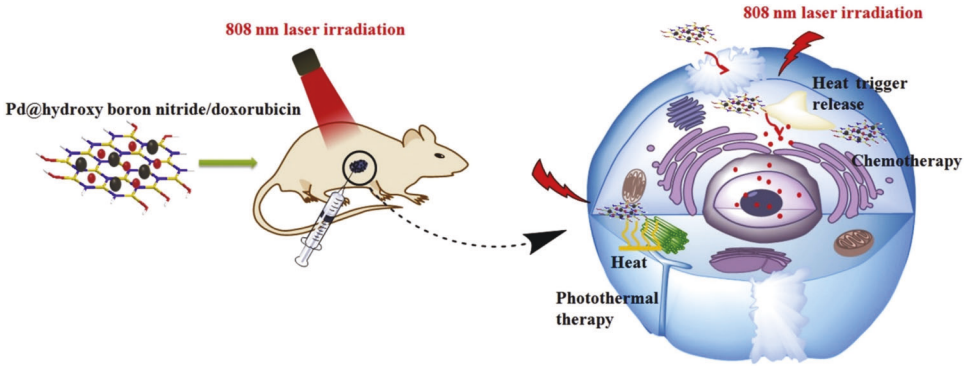

FIG. 15. Schematic illustration of using Pd@OH-BNNS for heat triggered release of drug. Reproduced with permission from Zhang *et al.*, Colloids Surf., B **176**, 300–308 (2019). Copyright 2019 Elsevier Science.

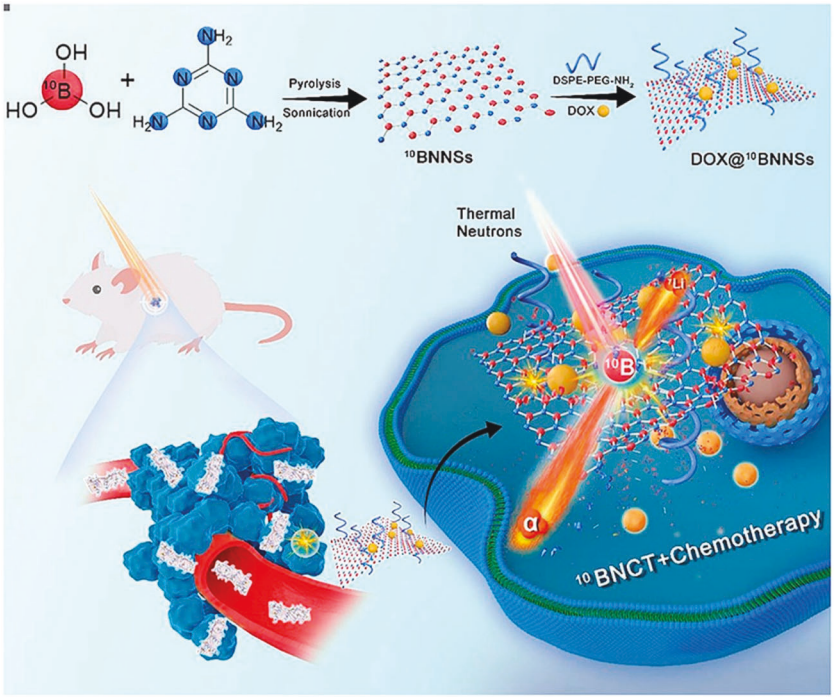

FIG. 16. Schematic illustration of a multimodal treatment using DOX@^{10}BNNSs. Reproduced with permission from Li *et al.*, Biomaterials **268**, 120587 (2021). Copyright 2021 Elsevier Science.

In another study, BNNSs are used to form a multifunctional nano-complex for synergistic chemotherapy and low-temperature photothermal therapy (PTT).[161] BNNSs were functionalized with cRGD peptide through functionalized PEG linkers and loaded with the chemotherapeutic drug DOX and a heat shock protein inhibitor (17AAG, allylamino-17-demethoxygeldanamycin). The resultant DOX-17AAG@B-PEG-cRGD complex shows both pH-controlled and near-infrared (NIR)-induced DOX and 17AAG release. The complex also enhanced cellular uptake in cancerous cells over healthy cells and inhibited the Hsp90 expression to reduce the heat tolerance of cancer cells. *In vitro* assays showed that treatment under NIR laser irradiation led to significant cell death, indicating enhanced therapeutic effects from combining PTT with chemotherapy. *In vivo*, biodistribution studies confirmed efficient tumor accumulation (12.3% targeting efficacy) and effective elimination of the nanocomposite.[161]

Qian *et al.* investigated BNNSs functionalized polycaprolactone (PCL) scaffold (Fig. 17) for peripheral nerve injury treatment, leveraging its piezoelectric properties to enhance nerve regeneration.[162] It is proposed that micro-electricity generated from the scaffold during mechanical stress facilitates Schwann cell migration, adhesion, and axonal extension, contributing to improved nerve repair. The evaluation of neovascularization using vessel maker CD34 showed significantly higher expression levels in the BNNS@PCL group, indicating enhanced vascular support compared to autografts and PCL scaffolds.[162]

F. Antibacterial applications

Xie *et al.* compared the biocompatibility of BNNSs with commercially available graphene quantum dots (GQDs).[163] They synthesized BNNSs through a ball milling process using h-BN powders and 6-aminocaproic acid, followed by sonication and filtration to create a 1 mg/ml aqueous solution. The hemolytic effects of varying concentrations of BNNSs and GQDs (both ~14–25 nm in lateral size and <2 nm thick) were evaluated on isolated red blood cells through an in vitro hemolysis experiment. The hemolysis percentages were calculated based on hemoglobin release measured by absorbance. BNNSs and GQDs perform equally well up to a 12.5 mg/ml concentration with ignorable hemolysis percentages. However, hemolysis increased at higher concentrations of BNNSs and reached ~20% at 200 mg/ml, while hemolysis remained low for GQDs. MD simulation suggests BNNSs can penetrate the cell membrane and extract phospholipid molecules directly from the lipid bilayer. The penetration effect of BNNSs was thermodynamically favorable due to the strong, attractive van der Waals interactions between BNNSs and phospholipids.

Nano cytotoxicity at a high loading level can be used for biomedical applications, such as degrading bacterial membranes, particularly those of *Escherichia coli* (*E. coli*).[164] Experiments and MD simulations show that BNNSs interact with the membranes (Fig. 18), extracting lipids and causing membrane deformation.[165] This leads to a loss of membrane integrity, with the outer membrane being more vulnerable than the inner membrane. The lipid extraction process is spontaneous and contributes to increased membrane rigidity and cell death.

Ikram *et al.* compared pure BNNSs with Zr-doped BNNSs for antibacterial properties, which exhibits significant agglomeration and Zr decoration.[166] The antimicrobial action was investigated *in vitro* through inhibition zone measurements (mm) using an agar well diffusion assay against *S. aureus* and *E. coli*. Zr-doped BNNS demonstrated substantial antibacterial activity against both

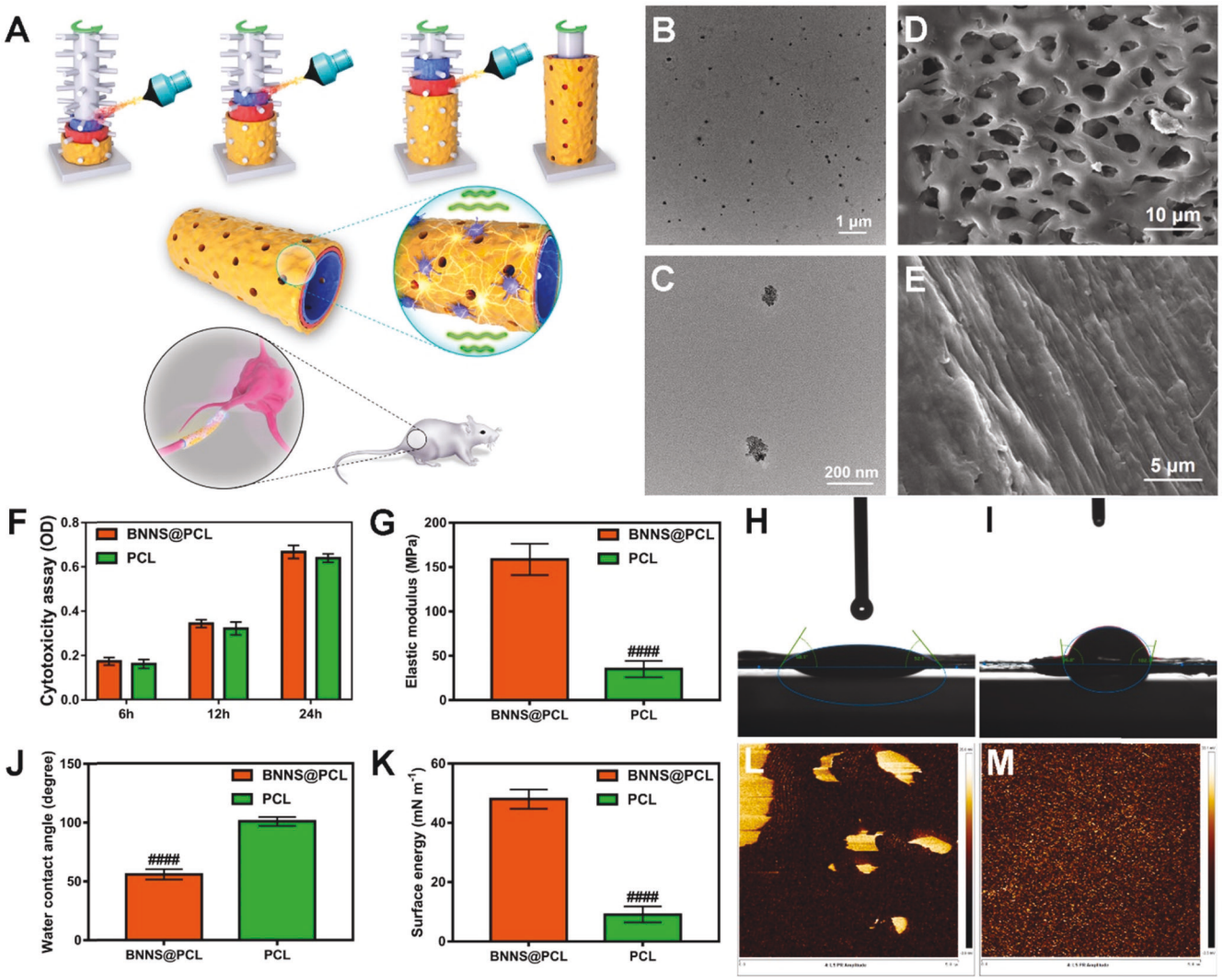

FIG. 17. (a) Fabrication of BNNS-functionalized PCL channel scaffold using a 3D layer-by-layer droplet spraying method, (b) and (c) BNNS morphology via transmission electron microscopy, (d) and (e) BNNS@PLC morphology via scanning electron microscopy, (f) cytotoxicity of BNNS@PCL and PCL on Schwann cells, (g) elastic modulus (MPa), (h) and (i) hydrophilicity of scaffolds, (j) water contact angle (degrees), (k) surface energy (mN m^{-1}), and (l) and (m) piezoelectric properties via piezo-response force microscopy. Reproduced with permission from Qian *et al.*, Nano Energy **83**, 105779 (2021). Copyright 2021 Elsevier Science.

S. aureus and *E. coli*, with inhibition zones increasing with higher Zr concentrations.

BN composites were also studied for their antimicrobial properties. Guan *et al.* simultaneously exfoliated and functionalized h-BN via mixed ball milling with polysaccharide [carboxymethyl cellulose (CMC)] and soy protein isolate (SPI).[167] The CMC-SPI-BNNS composite demonstrated improved stability and antibacterial activity, achieving an inhibition zone against *E. coli* of 17.0 mm with a minimal inhibitory concentration (MIC) of ~0.8 mg ml^{-1}. A study also investigated the antibacterial and antifungal properties of BN films loaded with gentamicin and amphotericin B. The BN films promoted the sustained release of antibiotics in phosphate-buffered saline (PBS) solution, with G150/BN achieving a remarkable 99.99% reduction of *E. coli* at low concentrations after 24 h. Transmission electron microscopy analysis revealed that the sharp nanostructures of BN physically damage bacterial membranes, contributing to cell death.

On the other hand, generating reactive oxygen species (ROS) enhances the bactericidal effect.[168] Gudz *et al.* demonstrated that Gram-negative antibiotic-resistant *E. coli* bacteria are physically destructed when contacting BNNSs/nanoneedle decorated h-BN surfaces. The BN films loaded with a mixture of gentamicin (150 and 300 $\mu g/cm^2$) and amphotericin B (100 $\mu g/cm^2$) effectively inhibit the growth of *E. coli* K-261 and *Neurospora crassa* strains. During

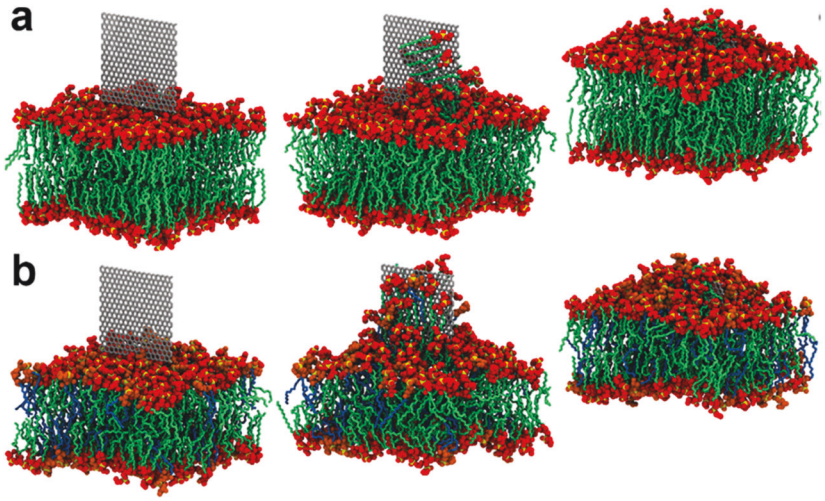

FIG. 18. Simulations using MD validated the extraction of lipids. (a) Outer_GramN-BNNS and (b) inner_GramN-BNNS systems' snapshots at 0, 50, and 500 ns. Reproduced with permission from Zhang *et al.*, Langmuir **35**(18), 6179–6187 (2019). Copyright 2019 American Chemical Society.

immersion in the normal saline solution, the BN film generates ROS to accelerate oxidative stress at the cell contact points. The obtained results are valuable for further developing nanostructured surfaces with contact killing, ROS, and biocide release abilities.

Various nonwoven fibrous membranes have been studied for their PM2.5 removal efficiency and antibacterial activities. Xiong *et al.* covalently immobilized quaternary ammonium salt (QAC) on the surfaces of plasma-hydroxylated h-BN nanoparticles.[169] Melt-blown polypropylene (PP) ultrafine fiber nonwovens were treated with oxygen plasma to activate their surface and then soaked in the QAC/h-BN nanoplatelet suspension. The wet QAC/h-BN/PP composite nonwovens were dried and hot-pressed to obtain QAC/h-BN/PP nanocomposite fibrous membranes. The QAC/h-BN/PP membranes showed antibacterial rates of 99.3% for *E. coli* and 96.1% for *S. aureus*, based on "contact killing" without releasing unfavorable biocides (Fig. 19).[169]

Research has shown that h-BN nanoparticles are antimicrobial, antibiofilm, and cytocompatible at 0.025–0.1 mg/ml, showing their potential in antibacterial and biocompatible applications. While

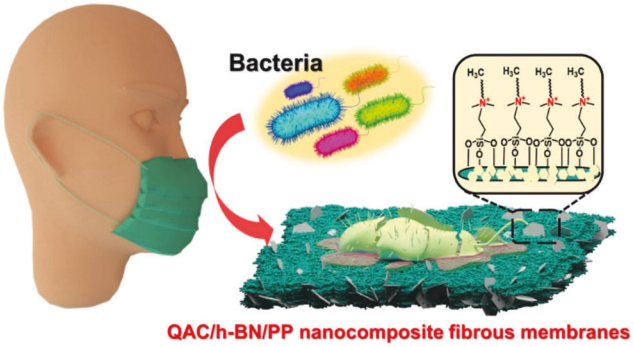

FIG. 19. Antibacterial mechanism of QAC/h-BN/PP nanocomposite fibrous masks. Reproduced with permission from Xiong *et al.*, ACS Appl. Mater. Interfaces **13**(1), 196–206 (2021). Copyright 2021 American Chemical Society.

h-BN nanoparticles inhibit bacterial biofilm without cell death, h-BN nanoflakes disrupt bacterial membranes,[170] leading to cell lysis due to the sharp edges.[165,171]

A study also explored the antibacterial properties of BNNSs against multidrug-resistant bacteria and compared their toxicity with silver nanoparticles. BNNSs showed 99% clearance from the lungs within 7 days. BNNSs exhibited potent antibacterial activity against five multidrug-resistant strains without including antimicrobial resistance, which employs a distinct killing mechanism by impairing Z-ring constriction.[172] Another study found that h-BN nanoparticles had no antiviral effect on Bovine Coronavirus (BCoV) and showed slight toxicity on HRT-18 cells. However, the coated fabric of boron nitride nanoparticles significantly improved bacterial filtration against *Staphylococcus aureus*.[173] Composites of functionalized BNNSs, graphene oxide, and silver (FBN–GO–Ag) nanocomposites improved the separation and antibacterial properties of polyether sulfone membranes in wastewater treatment. The composites enhanced the membrane's porosity, permeability, and antibacterial performance. 0.5 wt. % FBN-GO-Ag membrane exhibited a high flux recovery ratio (FRR) of 83.6%, with increased hydrophilicity and lower surface roughness, which resulted in superior antifouling and antibacterial properties, effectively inhibiting *E. coli* growth.[174]

The biodegradation of h-BN was studied based on the boron precursor used in the synthesis methods. It was shown that h-BN synthesized from colemanite is more resistant to degradation (at 30 days), while those made by boric acid or boron trioxide were more prone to degradation.[175,176] Hammi *et al.* prepared boron nitride-filled chitosan films (CS-BN_x-f) by mixing water-soluble chitosan with dispersed h-BN to get flexible and stable films containing 60 wt. % BN. These CS-BN_x-f films demonstrated antibacterial activity against *E. coli* and *S. aureus*, along with improved surface hydrophobicity and antibacterial capacity, making these films antibacterial, flame-retardant, and moisture-resistant materials.[177] Boron nitride films were very helpful antimicrobial materials for multidrug-resistant pathogens. h-BN utilizes mechanisms such as oxidative stress and cell membrane disruption to target microbes.[178]

G. High-brightness probes (HBPs) by BN dots for fluorescence *in situ* hybridization

We recently created BN dots as nanocarriers to conjugate with desired organic dyes and single-stranded deoxyribonucleic acids (ssDNAs) to form high-brightness probes (HBPs) for gene sequence detection.[13] As discussed in the introduction, BN dots differ from BN QDs reported by others. BN QDs have self-fluorescence, which will become background noise and does not apply to fluorescent probes. In contrast, BN dots are not fluorescent, allowing us to conjugate with desired organic dye molecules to produce strong fluorescence signals at desired wavelengths.

Figure 20(a) shows the schematics of a HBP with a series of FAM dye molecules (fluorescein) and an ssDNA probe (StabiLux 495 probes) of 20 nucleotides (nt).[179,180] For fluorescence *in situ* hybridization (FISH) experiments, a target RNA [green line in Fig. 20(b)] is first hybridized with 30–50 primary oligo probes (orange lines), each with 35 nt of complementary sequences (CSs) to the target. Each primary probe has a bridging tail (the sticking end) with a series of 20 nt complementary to the ssDNA probes of the HBPs (green dots with blue lines).

The authors hybridized StabiLux 495 probes with streptavidin agarose beads to prove the concept. StabiLux 495 probes were conjugated with biotinylated complementary DNA sequence (CS) and

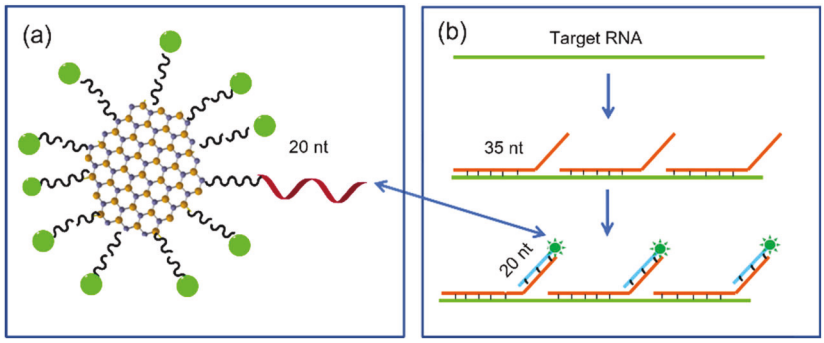

FIG. 20. (a) Schematic of a StabiLux 495 secondary FISH probe. (b) Schematic of FISH workflow.

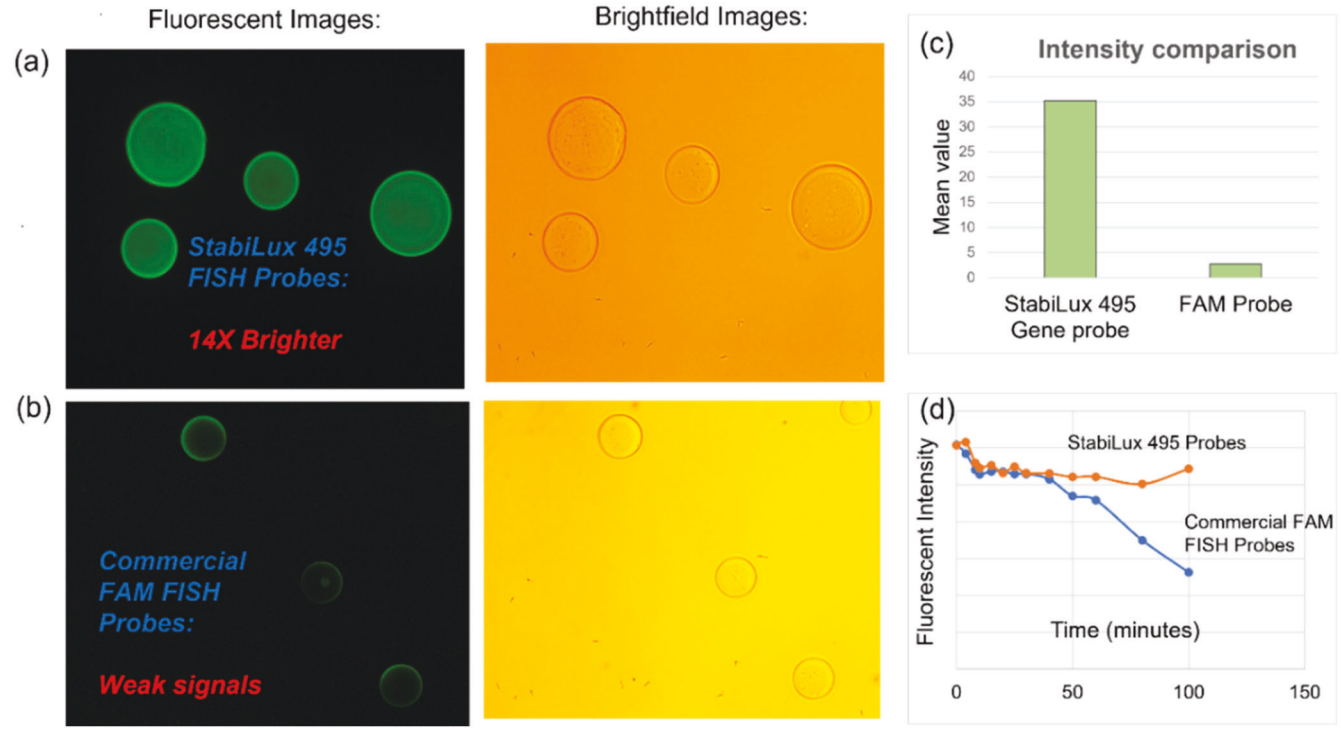

FIG. 21. Fluorescent and brightfield images of microbeads stained with (a) StabiLucx 495 FISH probes and (b) commercial FAM FISH probes. (c) Brightness and (d) photostability comparison between the two types of FISH probes.

biotinylated non-complementary DNA sequence (NCS) as a control. Both samples are then incubated and captured by streptavidin agarose beads. Figure 21(a) shows the fluorescence of the capture beads stained with StabiLux 495 FISH probes is much brighter than those stained with the commercial FAM FISH probes [Fig. 21(b)]. We further qualified and compared the brightness using *ImageJ* software. As shown in Fig. 21(c), these results demonstrate that StabiLux 495 FISH probes are at least 14× brighter than commercial FAM FISH probes. In addition, StabiLux 495 FISH probes are >2× more photostable than FAM dye [Fig. 21(d)].

The authors reported specific binding on ACTB mRNAs in the HeLa cells. As quantified by the *ImageJ* software (not shown here), StabiLux FISH probes specifically stained on the primary and the target are 10× brighter (signal = 2724) than the commercial FAM FISH probes (signal = 263), even when imaged with a charge-coupled device (CCD) camera without an electron-multiplying charge-coupled device (EMCCD).

V. SUMMARY AND PERSPECTIVE

In Secs. II–IV, we have reviewed the properties, synthesis methods, and biomedical applications of BNNSs, BN QDs, and BN dots. In the following three paragraphs, let us summarize these three areas and provide some perspectives for future research.

Due to their large bandgap (6 eV), BNNSs retain the properties of h-BN, being electrically insulating and optically transparent. Because of the sp^2 hexagonal networks, BNNSs are mechanically strong such as graphene, enabling their usage in mechanical reinforcement, such as bone tissue engineering. In contrast, BN QDs are nanoscale (lateral dimension < 10 nm) BNNSs but with contamination. The literature suggests that BN QDs contain carbon, oxygen, and hydrogen atoms, leading to excitation-dependent emission (fluorescence) in a broad spectra range of ~350–550 nm. Excitation-dependent emission can be convenient for imaging applications but could also be undesired as intense background noises. Again, such shrinking in the optical gap is not due to the quantum confinement effect. Therefore, it is weird to call BN QDs quantum dots. In contrast, BN dots are the real nanoscale version of BNNSs, retaining the electrically insulating and optically transparent nature without undesired noise fluorescence. Future property research should focus on two directions: (1) What is the structural origin of excitation-dependent emission in BN QDs? What is the bonding nature of carbon, oxygen, and hydrogen on BN that causes such interesting fluorescence? This would lead to a new understanding of making new fluorophores; and (2) modify the intrinsic property of BNNSs, BN QDs, and BN dots. For example, functionalize the hydrophobic BNNSs with a hydroxyl group to enhance dispersity in biomedical applications such as $BN(OH)_x$ discussed in Sec. IV A 1. Another example would be labeling the non-fluorescent BN dots with the desired organic dye to enable specific fluorescence, as demonstrated for HBPs for gene sequence detection.[13,179,180]

In terms of synthesis, there are many top-down and bottom-up methods for producing BNNSs, BN QDs, and BN dots. This is not unique to nanomaterial research but also happens in other 2D materials such as graphene and TMDs. As always, future research should focus on (1) quality control and (2) scalability (production yield). For example, producing wafer-scale BNNSs on gold films will enable BNNSs to be used in graphene and TMD electronics (beyond the scope of this review).[181] Similar techniques are needed for the scalable production of suspended BNNSs, BN QDs, and BN dots for biomedical applications. In addition to scalability, it is desired to gain control of the product quality; for example, lateral dimension and thickness of BNNSs are still polydisperse, which may affect large-scale and reproducible applications.

Last but not least, applications are always the driving force of material research. Promising applications could even lead to the commercial use of BNNSs, BN QDs, and BO dots, which are highly desired to advance the field. Researchers should focus on studying unique applications that can only be enabled by using these BN nanostructures. For example, BNCT using BNNSs containing ^{10}B elements combined with chemotherapy drug delivery (DOX@BNNSs)[160] discussed in Sec. IV E is unique and impossible with graphene and TMDs. Another example would be using BN dots' electrically insulating and optically transparent nature to make HBPs for gene sequence detection (Sec. IV G). Such wide bandgap properties prevent fluorescent quenching and reduce the optical loss of the organic dye conjugated on each BN dot. This leads to high fluorescent brightness,[13,179,180] which is not achievable by metallic graphene. Other unique properties of BN nanomaterials, such as piezoelectricity, are also worth considering when designing new biomedical applications.

ACKNOWLEDGMENTS

The authors acknowledge the support from the National Science Foundation (Award Nos. 2034693 and 2329746).

AUTHOR DECLARATIONS

Conflict of Interest

The authors have no conflicts to disclose.

Author Contributions

R.D., Z.S., X.L., N.Y., R.O., D.Z., and Y.K.Y. drafted and contributed the sections on biomedical applications. M.C. drafted the section on synthesis methods. J.U. and Y.K.Y. drafted the sections on the introduction and properties. Y.K.Y. planned, edited, and finalized the full paper. All authors reviewed the final paper.

Raksha Dubey: Project administration (equal); Writing – original draft (equal); Writing – review & editing (equal). **Matthew Cowles**: Writing – original draft (equal); Writing – review & editing (equal). **Zohreh Salimi**: Writing – original draft (equal); Writing – review & editing (equal). **Xiuling Liu**: Funding acquisition (equal); Writing – original draft (equal); Writing – review & editing (equal). **Rodney Oakley**: Writing – original draft (equal); Writing – review & editing (equal). **Nazmiye Yapici**: Funding acquisition (equal); Writing – original draft (equal); Writing – review & editing (equal). **Join Uddin**: Writing – original draft (equal); Writing – review & editing (equal). **Dongyan Zhang**: Conceptualization (equal); Funding acquisition (equal); Writing – original draft (equal); Writing – review & editing (equal). **Yoke Khin Yap**: Conceptualization (lead); Funding acquisition (equal); Project administration (lead); Supervision (lead); Writing – original draft (equal); Writing – review & editing (lead).

DATA AVAILABILITY

Data sharing is not applicable to this article as no new data were created or analyzed in this study.

REFERENCES

[1] D. Pacilé, J. C. Meyer, Ç. Ö. Girit, and A. Zettl, Appl. Phys. Lett. **92**(13), 133107 (2008).
[2] W.-Q. Han, L. Wu, Y. Zhu, K. Watanabe, and T. Taniguchi, Appl. Phys. Lett. **93**(22), 223103 (2008).
[3] L. Song, L. Ci, H. Lu, P. B. Sorokin, C. Jin, J. Ni, A. G. Kvashnin, D. G. Kvashnin, J. Lou, B. I. Yakobson, and P. M. Ajayan, Nano Lett. **10**(8), 3209–3215 (2010).
[4] J. C. Meyer, A. Chuvilin, G. Algara-Siller, J. Biskupek, and U. Kaiser, Nano Lett. **9**(7), 2683–2689 (2009).
[5] K. S. Novoselov, A. K. Geim, S. V. Morozov, D. Jiang, Y. Zhang, S. V. Dubonos, I. V. Grigorieva, and A. A. Firsov, Science **306**(5696), 666–669 (2004).
[6] A. Splendiani, L. Sun, Y. Zhang, T. Li, J. Kim, C.-Y. Chim, G. Galli, and F. Wang, Nano Lett. **10**(4), 1271–1275 (2010).
[7] J. N. Coleman, M. Lotya, A. O'Neill, S. D. Bergin, P. J. King, U. Khan, K. Young, A. Gaucher, S. De, R. J. Smith, I. V. Shvets, S. K. Arora, G. Stanton, H.-Y. Kim, K. Lee, G. T. Kim, G. S. Duesberg, T. Hallam, J. J. Boland, J. J. Wang, J. F. Donegan, J. C. Grunlan, G. Moriarty, A. Shmeliov, R. J. Nicholls, J. M. Perkins, E. M. Grieveson, K. Theuwissen, D. W. McComb, P. D. Nellist, and V. Nicolosi, Science **331**(6017), 568–571 (2011).
[8] Y. Xi, M. Zhao, X. Wang, S. Li, X. He, Z. Wang, and H. Bu, J. Phys. Chem. C **115**(36), 17743–17749 (2011).
[9] L. Lin, Y. Xu, S. Zhang, I. M. Ross, A. C. M. Ong, and D. A. Allwood, Small **10**(1), 60–65 (2014).
[10] V. Štengl, J. Henych, and M. Kormunda Sci. Adv. Mater. **6**(6) 1106–1116 (2014).
[11] A. Acharya, S. Sharma, X. Liu, D. Zhang, and Y. K. Yap, C **7**(2), 35 (2021).
[12] J. Uddin, R. Dubey, V. S. Balasubramaniam, J. Kabel, V. Khare, Z. Salimi, S. Sharma, D. Zhang, and Y. K. Yap, Micromachines **15**(3), 349 (2024).
[13] Y. K. Yap, D. Zhang, A. Acharya, N. Yapici, and X. Liu, "High-brightness nanodot fluorophores by covalent functionalization," United States Patent Application (US 2022/0226509 A1) (Jul 21, 2022).
[14] Y. K. Yap, "Boron-Carbon Nitride Nanohybrids," Encycl. Nanosci. Nanotechnol. **1**, 383–394 (2004).
[15] C. H. Lee, V. K. Kayastha, J Wang, and Y. K. Yap, "Introduction to B–C–N Materials," in *In B-C-N Nanotubes and Related Nanostructures.* Lecture Notes in Nanoscale Science and Technology, 6 (Springer, New York, NY, 2009).
[16] G. Lu, T. Wu, Q. Yuan, H. Wang, H. Wang, F. Ding, X. Xie, and M. Jiang, Nat. Commun. **6**, 6160 (2015).
[17] H. Liu, M. Yan, W. Jing, G. Zeng, G. Xie, X. Pu, Y. Fu, X. Peng, H. Wang, C. Lai, D. Huang, and L. Tang, Diamond Relat. Mater. **148**, 111410 (2024).
[18] A. Zunger, A. Katzir, and A. Halperin, Phys. Rev. B **13**(12), 5560–5573 (1976).
[19] X. Zhong, Y. K. Yap, R. Pandey, and S. P. Karna, Phys. Rev. B **83**(19), 193403 (2011).
[20] R. Beiranvand and S. Valedbagi, Diamond Relat. Mater. **58**, 190–195 (2015).
[21] S. Ma, C. Jiang, Q. Song, J. Chen, J. Xiao, and Q. Wei, J. Electron. Mater. **51**(4), 1663–1668 (2022).
[22] S. Angizi, S. A. A. Alem, M. Hasanzadeh Azar, F. Shayeganfar, M. I. Manning, A. Hatamie, A. Pakdel, and A. Simchi, Prog. Mater. Sci. **124**, 100884 (2022).
[23] L. Liu, Z. Xiong, D. hu, G. Wu, B. Liu, and P. Chen, Chem. Lett. **42**, 1415–1416 (2013).
[24] Z. Lin, A. McNamara, Y. Liu, K.-s. Moon, and C. P. Wong, Compos. Sci. Technol. **90**, 123–128 (2014).
[25] L. H. Li, Y. Chen, G. Behan, H. Zhang, M. Petravic, and A. M. Glushenkov, J. Mater. Chem. **21**(32), 11862–11866 (2011).
[26] Y. Yao, Z. Lin, Z. Li, X. Song, K.-S. Moon, and C.-p. Wong, J. Mater. Chem. **22**(27), 13494–13499 (2012).
[27] D. Fan, J. Feng, J. Liu, T. Gao, Z. Ye, M. Chen, and X. Lv, Ceram. Int. **42**, 7155 (2016).
[28] C. Cao, Y. Xue, Z. Liu, Z. Zhou, J. Ji, Q. Song, Q. Hu, Y. Fang, and C. Tang, 2D Mater. **6**, 035014 (2019).
[29] S. Chen, R. Xu, J. Liu, X. Zou, L. Qiu, F. Kang, B. Liu, and H.-M. Cheng, Adv. Mater. **31**(10), 1804810 (2019).
[30] K. R. Paton, E. Varrla, C. Backes, R. J. Smith, U. Khan, A. O'Neill, C. Boland, M. Lotya, O. M. Istrate, P. King, T. Higgins, S. Barwich, P. May, P. Puczkarski, I. Ahmed, M. Moebius, H. Pettersson, E. Long, J. Coelho, S. E. O'Brien, E. K. McGuire, B. M. Sanchez, G. S. Duesberg, N. McEvoy, T. J. Pennycook, C. Downing, A. Crossley, V. Nicolosi, and J. N. Coleman, Nat. Mater. **13**(6), 624–630 (2014).
[31] E. Varrla, C. Backes, K. R. Paton, A. Harvey, Z. Gholamvand, J. McCauley, and J. N. Coleman, Chem. Mater. **27**(3), 1129–1139 (2015).
[32] E. Varrla, K. R. Paton, C. Backes, A. Harvey, R. J. Smith, J. McCauley, and J. N. Coleman, Nanoscale **6**(20), 11810–11819 (2014).
[33] F. I. Alzakia and S. C. Tan, Adv. Sci. **8**(11), 2003864 (2021).
[34] O. Hod, J. Chem. Theory Comput. **8**(4), 1360–1369 (2012).
[35] C. Tan, X. Cao, X.-J. Wu, Q. He, J. Yang, X. Zhang, J. Chen, W. Zhao, S. Han, G.-H. Nam, M. Sindoro, and H. Zhang, Chem. Rev. **117**(9), 6225–6331 (2017).
[36] Y. Wang and Y. Ni, Anal. Chem. **86**(15), 7463–7470 (2014).
[37] C.-X. Hu, Y. Shin, O. Read, and C. Casiraghi, Nanoscale **13**(2), 460–484 (2021).
[38] H. Li, R. Y. Tay, S. H. Tsang, X. Zhen, and E. H. T. Teo, Small **11**(48), 6491–6499 (2015).
[39] Q. Liu, C. Hu, and X. Wang, Mater. Lett. **234**, 306–310 (2019).
[40] L. Chen, X. Zhang, Z. Zhao, F. Wang, Y. Huang, C. Bai, L. An, and Y. Yu, Colloids Surf., A **614**, 126181 (2021).
[41] R. Kumar, R. K. Singh, S. K. Yadav, R. Savu, and S. A. Moshkalev, J. Alloys Compd. **683**, 38 (2016).
[42] Y. Lin and J. W. Connell, Nanoscale **4**(22), 6908–6939 (2012).
[43] Q. Cao, F. Grote, M. Huβmann, and S. Eigler, Nanoscale Adv. **3**(4), 963–982 (2021).
[44] X. Zhang, L. An, C. Bai, L. Chen, and Y. Yu, Mater. Today Chem. **20**, 100425 (2021).
[45] D. Peng, L. Zhang, F.-F. Li, W.-R. Cui, R.-P. Liang, and J.-D. Qiu, ACS Appl. Mater. Interfaces **10**(8), 7315–7323 (2018).
[46] N. I. Kovtyukhova, Y. Wang, R. Lv, M. Terrones, V. H. Crespi, and T. E. Mallouk, J. Am. Chem. Soc. **135**(22), 8372–8381 (2013).
[47] H. Liang, B. Cao, J. Zhu, X. Shen, M. Zhu, B. Geng, P. Zhang, S. Zhu, F. Yu, R. Zhang, H. Tang, Q. Yuan, J. Li, W. Li, and Y. Chen, Appl. Surf. Sci. **604**, 154118 (2022).
[48] B. W. Reed, C. Tran, and K. J. Koski, Phys. Rev. Mater. **7**(4), 044003 (2023).
[49] B. Yu, J. Fan, J. He, Y. Liu, R. Wang, K. Qi, P. Han, and Z. Luo, J. Alloys Compd. **930**, 167303 (2023).
[50] L. Yu, P. L. Yap, D. N. H. Tran, A. M. C. Santos, and D. Losic, Nanotechnology **32**(40), 405601 (2021).
[51] J. Rawat, D. Sajwan, S. V. Garimella, H. Sharma, and C. Dwivedi, Nano Trends **2**, 100008 (2023).
[52] M. Liu, Y. Xu, Y. Wang, X. Chen, X. Ji, F. Niu, Z. Song, and J. Liu, Adv. Opt. Mater. **5**, 1600661 (2017).
[53] H. Xing, Q. Zhai, X. Zhang, J. Li, and E. Wang, Anal. Chem. **90**(3), 2141–2147 (2018).
[54] Z. Lei, S. Xu, J. Wan, and P. Wu, Nanoscale **7**(45), 18902–18907 (2015).
[55] Y. Ding, P. He, S. Li, B. Chang, S. Zhang, Z. Wang, J. Chen, J. Yu, S. Wu, H. Zeng, and L. Tao, ACS Nano **15**(9), 14610–14617 (2021).
[56] W. Lei, V. N. Mochalin, D. Liu, S. Qin, Y. Gogotsi, and Y. Chen, Nat. Commun. **6**(1), 8849 (2015).
[57] L. Wang, Q. Zhang, P. Su, L. Yu, Y. Bu, C. Yuan, and S. Wang, Anal. Chim. Acta **1236**, 340585 (2022).
[58] S. C. Singh, S. K. Mishra, R. K. Srivastava, and R. Gopal, J. Phys. Chem. C **114**(41), 17374–17384 (2010).
[59] S.-L. Hu, K.-Y. Niu, J. Sun, J. Yang, N.-Q. Zhao, and X.-W. Du, J. Mater. Chem. **19**(4), 484–488 (2009).
[60] E. Fazio, B. Gökce, A. De Giacomo, M. Meneghetti, G. Compagnini, M. Tommasini, F. Waag, A. Lucotti, C. G. Zanchi, P. M. Ossi, M. Dell'Aglio, L. D'Urso, M. Condorelli, V. Scardaci, F. Biscaglia, L. Litti, M. Gobbo, G. Gallo, M. Santoro, S. Trusso, and F. Neri, Nanomaterials **10**, 2317 (2020).

[61]H. Muneoka, T. Koike, T. Ito, K. Terashima, and E. Miura, J. Phys. D: Appl. Phys. **57**, 245205 (2024).
[62]V. Nguyen, L. Yan, N. Zhao, N. Van Canh, N. T. N. Hang, and P. H. Le, J. Mol. Struct. **1244**, 130922 (2021).
[63]Y. Xu, L. Yan, J. Si, and N. Zhao, "Femtosecond laser-assisted fabrication of fluorescent boron nitride quantum dots," in *2019 IEEE International Conference on Manipulation, Manufacturing and Measurement on the Nanoscale (3M-NANO)* (IEEE, 2019).
[64]B. C. Garrett, D. A. Dixon, D. M. Camaioni, D. M. Chipman, M. A. Johnson, C. D. Jonah, G. A. Kimmel, J. H. Miller, T. N. Rescigno, P. J. Rossky, S. S. Xantheas, S. D. Colson, A. H. Laufer, D. Ray, P. F. Barbara, D. M. Bartels, K. H. Becker, K. H. Bowen, Jr., S. E. Bradforth, I. Carmichael, J. V. Coe, L. R. Corrales, J. P. Cowin, M. Dupuis, K. B. Eisenthal, J. A. Franz, M. S. Gutowski, K. D. Jordan, B. D. Kay, J. A. LaVerne, S. V. Lymar, T. E. Madey, C. W. McCurdy, D. Meisel, S. Mukamel, A. R. Nilsson, T. M. Orlando, N. G. Petrik, S. M. Pimblott, J. R. Rustad, G. K. Schenter, S. J. Singer, A. Tokmakoff, L.-S. Wang, and T. S. Zwier, Chem. Rev. **105**(1), 355–390 (2005).
[65]M. Pshenichnikov, A. Baltuška, and D. Wiersma, Chem. Phys. Lett. **389**, 171 (2004).
[66]Muttaqin, T. Nakamura, and S. Sato, Appl. Phys. A **120**, 881 (2015).
[67]T. Ito, T. Goto, K. Inoue, K. Ishikawa, H. Kondo, M. Hori, Y. Shimizu, Y. Hakuta, and K. Terashima, Appl. Phys. Express **13**, 066001 (2020).
[68]K. Inoue, T. Goto, T. Ito, Y. Shimizu, Y. Hakuta, K. Ito, and K. Terashima, J. Phys. D: Appl. Phys. **54**(42), 425202 (2021).
[69]M. Molaei, M. Younas, and M. Rezakazemi, ACS Appl. Electron. Mater. **3**, 5165 (2021).
[70]A. E. Naclerio and P. R. Kidambi, Adv. Mater. **35**(6), 2207374 (2023).
[71]A. Pakdel, C. Zhi, Y. Bando, T. Nakayama, and D. Golberg, ACS Nano **5**(8), 6507–6515 (2011).
[72]J. Xu, C.-S. Lee, Y.-B. Tang, X. Chen, Z.-H. Chen, W.-J. Zhang, S.-T. Lee, W. Zhang, and Z. Yang, ACS Nano **4**(4), 1845–1850 (2010).
[73]L. Qin, J. Yu, M. Li, F. Liu, and X. Bai, Nanotechnology **22**(21), 215602 (2011).
[74]Y. Zhu, Y. Bando, L. Yin, and D. Golberg, Nano Lett. **6**(12), 2982–2986 (2006).
[75]Z.-G. Chen and J. Zou, J. Mater. Chem. **21**(4), 1191–1195 (2011).
[76]Z.-G. Chen, J. Zou, G. Liu, F. Li, Y. Wang, L. Wang, X.-L. Yuan, T. Sekiguchi, H.-M. Cheng, and G. Q. Lu, ACS Nano **2**, 2183–2191 (2008).
[77]G. Lian, X. Zhang, M. Tan, S. Zhang, D. Cui, and Q. Wang, J. Mater. Chem. **21**(25), 9201–9207 (2011).
[78]X. Wang, C. Zhi, L. Li, H. Zeng, C. Li, M. Mitome, D. Golberg, and Y. Bando, Adv. Mater. **23**(35), 4072–4076 (2011).
[79]Y. Kong, Y. He, J. Zhou, S. Zhong, and G. Song, ChemistrySelect **5**(13), 3828–3834 (2020).
[80]Ö. Tuna, Z. Balta, and E. B. Simsek, Chem. Eng. J. **474**, 145770 (2023).
[81]E. Bilgin Simsek, Ceram. Int. **48**, 26487 (2022).
[82]G. M. L. Consoli, L. Maugeri, N. Musso, A. Gulino, L. D'Urso, P. Bonacci, G. Buscarino, G. Forte, and S. Petralia, Adv. Healthcare Mater. **13**(16), 2303692 (2024).
[83]K. Ren, W. Zhao, Z. Zhai, T. Han, and H. Shi, Appl. Surf. Sci. **562**, 150144 (2021).
[84]A. Alrebh and J.-L. Meunier, 2D Mater. **8**(4), 045018 (2021).
[85]F. Liu, R. Han, S. Naficy, G. Casillas, X. Sun, and Z. Huang, ACS Appl. Nano Mater. **4**(8), 7988–7994 (2021).
[86]Y. Shi, C. Hamsen, X. Jia, K. K. Kim, A. Reina, M. Hofmann, A. L. Hsu, K. Zhang, H. Li, Z.-Y. Juang, M. S. Dresselhaus, L.-J. Li, and J. Kong, Nano Lett. **10**(10), 4134–4139 (2010).
[87]P. Sutter, J. Lahiri, P. Albrecht, and E. Sutter, ACS Nano **5**(9), 7303–7309 (2011).
[88]R. Wang, D. G. Purdie, Y. Fan, F. C. P. Massabuau, P. Braeuninger-Weimer, O. J. Burton, R. Blume, R. Schloegl, A. Lombardo, R. S. Weatherup, and S. Hofmann, ACS Nano **13**(2), 2114–2126 (2019).
[89]K. K. Kim, A. Hsu, X. Jia, S. M. Kim, Y. Shi, M. Hofmann, D. Nezich, J. F. Rodriguez-Nieva, M. Dresselhaus, T. Palacios, and J. Kong, Nano Lett. **12**(1), 161–166 (2012).
[90]L. Wang, B. Wu, J. Chen, H. Liu, P. Hu, and Y. Liu, Adv. Mater. **26**(10), 1559–1564 (2014).
[91]R. Y. Tay, X. Wang, S. H. Tsang, G. C. Loh, R. S. Singh, H. Li, G. Mallick, and E. H. Tong Teo, J. Mater. Chem. C **2**(9), 1650–1657 (2014).
[92]W. Auwärter, H. U. Suter, H. Sachdev, and T. Greber, Chem. Mater. **16**(2), 343–345 (2004).
[93]C. Zhang, L. Fu, S. Zhao, Y. Zhou, H. Peng, and Z. Liu, Adv. Mater. **26**(11), 1776–1781 (2014).
[94]R. Y. Tay, M. H. Griep, G. Mallick, S. H. Tsang, R. S. Singh, T. Tumlin, E. H. T. Teo, and S. P. Karna, Nano Lett. **14**(2), 839–846 (2014).
[95]K. Watanabe, T. Taniguchi, and H. Kanda, Nat. Mater. **3**(6), 404–409 (2004).
[96]T. Taniguchi, K. Watanabe, and S. Koizumi, Phys. Status Solidi A **201**, 2573–2577 (2004).
[97]Y. Kubota, K. Watanabe, and T. Taniguchi, Jpn. J. Appl. Phys. **46**(1R), 311 (2007).
[98]T. Taniguchi and K. Watanabe, J. Cryst. Growth **303**(2), 525–529 (2007).
[99]Y. Kobayashi, K. Kumakura, T. Akasaka, and T. Makimoto, Nature **484**(7393), 223–227 (2012).
[100]T. C. Doan, J. Li, J. Y. Lin, and H. X. Jiang, AIP Adv. **6**(7), 075213 (2016).
[101]T. C. Doan, S. Majety, S. Grenadier, J. Li, J. Y. Lin, and H. X. Jiang, Nucl. Instrum. Methods Phys. Res., Sect. A **748**, 84–90 (2014).
[102]A. Maity, T. C. Doan, J. Li, J. Y. Lin, and H. X. Jiang, Appl. Phys. Lett. **109**(7), 072101 (2016).
[103]T. C. Doan, S. Majety, S. Grenadier, J. Li, J. Y. Lin, and H. X. Jiang, Nucl. Instrum. Methods Phys. Res., Sect. A **783**, 121–127 (2015).
[104]A. R. Jang, S. Hong, C. Hyun, S. I. Yoon, G. Kim, H. Y. Jeong, T. J. Shin, S. O. Park, K. Wong, S. K. Kwak, N. Park, K. Yu, E. Choi, A. Mishchenko, F. Withers, K. S. Novoselov, H. Lim, and H. S. Shin, Nano Lett. **16**(5), 3360–3366 (2016).
[105]X. Li, S. Sundaram, Y. El Gmili, T. Ayari, R. Puybaret, G. Patriarche, P. L. Voss, J. P. Salvestrini, and A. Ougazzaden, Cryst. Growth Des. **16**(6), 3409–3415 (2016).
[106]W. Auwärter, M. Muntwiler, J. Osterwalder, and T. Greber, Surf. Sci. **545**(1), L735–L740 (2003).
[107]S. Chatterjee, Z. Luo, M. Acerce, D. M. Yates, A. T. C. Johnson, and L. G. Sneddon, Chem. Mater. **23**(20), 4414–4416 (2011).
[108]G. Dong, E. B. Fourré, F. C. Tabak, and J. W. M. Frenken, Phys. Rev. Lett. **104**(9), 096102 (2010).
[109]J. Yin, X. Liu, W. Lu, J. Li, Y. Cao, Y. Li, Y. Xu, X. Li, J. Zhou, C. Jin, and W. Guo, Small **11**(40), 5375–5380 (2015).
[110]A. Rice, A. Allerman, M. Crawford, T. Beechem, T. Ohta, C. Spataru, J. Figiel, and M. Smith, J. Cryst. Growth **485**, 90–95 (2018).
[111]S. Liu, B. Lu, Q. Zhao, J. Li, T. Gao, Y. Chen, Y. Zhang, Z. Liu, Z. Fan, F. Yang, L. You, and D. Yu, Adv. Mater. **25**(33), 4549–4554 (2013).
[112]M. Snure, Q. Paduano, and A. Kiefer, J. Cryst. Growth **436**, 16–22 (2016).
[113]M. Chubarov, H. Pedersen, H. Högberg, V. Darakchieva, J. Jensen, P. O. Å. Persson, and A. Henry, Phys. Status Solidi RRL **5**(10–11), 397–399 (2011).
[114]A. Nag, K. Raidongia, K. P. S. S. Hembram, R. Datta, U. V. Waghmare, and C. N. R. Rao, ACS Nano **4**(3), 1539–1544 (2010).
[115]Q. Li, Y. Zheng, X. Hou, T. Yang, T. Liang, and J. Zheng, Sens. Actuators, B **304**, 127353 (2020).
[116]W. Lei, D. Portehault, R. Dimova, and M. Antonietti, J. Am. Chem. Soc. **133**(18), 7121–7127 (2011).
[117]Z. Huang and T. Autrey, Energy Environ. Sci. **5**(11), 9257–9268 (2012).
[118]Y. Gu, M. Zheng, Y. Liu, and Z. Xu, J. Am. Ceram. Soc. **90**(5), 1589–1591 (2007).
[119]L. Tian, J. Li, F. Liang, S. Chang, H. Zhang, M. Zhang, and S. Zhang, J. Colloid Interface Sci. **536**, 664–672 (2019).
[120]J. Tzadikov, M. Auinat, J. Barrio, M. Volokh, G. Peng, C. Gervais, Y. Ein-Eli, and M. Shalom, ChemSusChem **11**(17), 2912–2920 (2018).
[121]R. H. Feng Liu, A. Nattestad, X. Sun, and Z. Huang, Surf. Innovations **9**(4), 222–230 (2021).
[122]M. Zhang, M. Zhou, Z. Luo, J. Zhang, S. Wang, and X. Wang, Chem. Commun. **56**(17), 2558–2561 (2020).
[123]Z. Luo, Y. Fang, M. Zhou, and X. Wang, Angew. Chem., Int. Ed. **58**(18), 6033–6037 (2019).
[124]X. Liu, M. Antonietti, and C. Giordano, Chem. Mater. **25**(10), 2021–2027 (2013).
[125]Z. L. Wu, P. Zhang, M. X. Gao, C. F. Liu, W. Wang, F. Leng, and C. Z. Huang, J. Mater. Chem. B **1**(22), 2868–2873 (2013).

[126]L. Wang, C. Sun, L. Xu, and Y. Qian, Catal. Sci. Technol. **1**(7), 1119–1123 (2011).
[127]B. Huo, B. Liu, T. Chen, L. Cui, G. Xu, M. Liu, and J. Liu, Langmuir **33**(40), 10673–10678 (2017).
[128]Q. Xue, H. Zhang, M. Zhu, Z. Wang, Z. Pei, Y. Huang, Y. Huang, X. Song, H. Zeng, and C. Zhi, RSC Adv. **6**(82), 79090–79094 (2016).
[129]R. Shankar, S. Marchesini, and C. Petit, J. Phys. Chem. C **123**(7), 4282–4290 (2019).
[130]L. Pizzorno, Integr. Med. (Encinitas) **14**(4), 35 (2015).
[131]Y. Zhang, H. G. Kang, H. z. Xu, H. Luo, M. Suzuki, Q. Lan, X. Chen, N. Komatsu, and L. Zhao, Adv. Mater. **35**(35), 2301479 (2023).
[132]S. M. Sharker, Int. J. Nanomed. **14**, 9983–9993 (2019).
[133]S. Mirón-Barroso, E. B. Domenech, and S. Trigueros, Int. J. Mol. Sci. **22**(16), 8537 (2021).
[134]G. Ailuno, A. Balboni, G. Caviglioli, F. Lai, F. Barbieri, I. Dellacasagrande, T. Florio, and S. Baldassari, Cells **11**(24), 4029 (2022).
[135]C. Wang, Y. Long, Y. Deng, Y. Han, D. Tishkevich, M. N. Ha, and Q. Weng, BMEMat **2**, e12068 (2024).
[136]Q. Weng, B. Wang, X. Wang, N. Hanagata, X. Li, D. Liu, X. Wang, X. Jiang, Y. Bando, and D. Golberg, ACS Nano **8**(6), 6123–6130 (2014).
[137]Y. Cheng, Y. Han, W. Zhang, L. Zeng, Y. Long, S. Wang, and Q. Weng, Chem. Eng. J. **437**, 135304 (2022).
[138]H. Hemmi, O. Takeuchi, T. Kawai, T. Kaisho, S. Sato, H. Sanjo, M. Matsumoto, K. Hoshino, H. Wagner, K. Takeda, and S. Akira, Nature **408**(6813), 740–745 (2000).
[139]J. Liu, T. Zheng, and Y. Tian, Angew. Chem., Int. Ed. **58**(23), 7757–7761 (2019).
[140]A. Rousseau, L. Ren, A. Durand, P. Valvin, B. Gil, K. Watanabe, T. Taniguchi, B. Urbaszek, X. Marie, C. Robert, and G. Cassabois, Nano Lett. **21**(23), 10133–10138 (2021).
[141]Y. Zhan, J. Yan, M. Wu, L. Guo, Z. Lin, B. Qiu, G. Chen, and K.-y. Wong, Talanta **174**, 365–371 (2017).
[142]M. Llenas, L. Cuenca, C. Santos, I. Bdikin, G. Gonçalves, and G. Tobías-Rossell, Biomedicines **10**(12), 3238 (2022).
[143]V. Kumar, K. Nikhil, P. Roy, D. Lahiri, and I. Lahiri, RSC Adv. **6**(53), 48025–48032 (2016).
[144]Q. Cai, L. H. Li, S. Mateti, A. Bhattacharjee, Y. Fan, S. Huang, and Y. I. Chen, Adv. Funct. Mater. **34**(40), 2403669 (2024).
[145]Y. Lu, R. Zhao, L. Wang, and S. E, Diamond Relat. Mater. **136**, 109978 (2023).
[146]A. Nadeem, M. A. Raza, M. F. Maqsood, M. T. Ilyas, A. Westwood, and Z. U. Rehman, Ceram. Int. **46**(12), 20415–20422 (2020).
[147]W. Sun, Y. Meng, Q. Fu, F. Wang, G. Wang, W. Gao, X. Huang, and F. Lu, ACS Appl. Mater. Interfaces **8**(15), 9881–9888 (2016).
[148]C. Shuai, Z. Han, P. Feng, C. Gao, T. Xiao, and S. Peng, J. Mater. Sci.:Mater. Med. **26**(5), 188 (2015).
[149]H. Li, L. Jing, R. Y. Tay, S. H. Tsang, J. Lin, M. Zhu, F. N. Leong, and E. H. T. Teo, Chem. Eng. J. **328**, 825–833 (2017).
[150]H. Belaid, S. Nagarajan, C. Barou, V. Huon, J. Bares, S. Balme, P. Miele, D. Cornu, V. Cavaillès, C. Teyssier, and M. Bechelany, ACS Appl. Bio Mater. **3**(4), 1865–1874 (2020).
[151]Z. Liu, A. Dibaji, D. Li, S. Mateti, J. Liu, F. Yan, C. J. Barrow, Y. Chen, K. Ariga, and W. Yang, Mater. Today **44**, 194–210 (2021).
[152]Z. Najafi, M. Kharaziha, F. Karimzadeh, and A. Shapiri, J. Appl. Polym. Sci. **138**(28), 50664 (2021).
[153]M. Ensoylu, A. M. Deliormanlı, and H. Atmaca, Biomimetics **8**(1), 10 (2022).
[154]M. Sekkarapatti Ramasamy, V. Krishnamoorthi Kaliannagounder, S. Ramasamy, V. Kumar, S. J. Park, S. S. Park, C. H. Park, S. S. Han, C. S. Kim, and B. Kim, J. Appl. Polym. Sci. **140**(43), e54598 (2023).
[155]A. Merlo, V. Mokkapati, S. Pandit, and I. Mijakovic, Biomater. Sci. **6**(9), 2298–2311 (2018).
[156]D. Döğan and A. Ü. Metin, Mater. Today Commun. **33**, 104807 (2022).
[157]D. V. Shtansky, A. T. Matveev, E. S. Permyakova, D. V. Leybo, A. S. Konopatsky, and P. B. Sorokinky, Nanomaterials **12**, 2810 (2022).
[158]Y. Zhang, R. Guo, D. Wang, X. Sun, and Z. Xu, Colloids Surf., B **176**, 300–308 (2019).
[159]G. Shim, S. Ko, J. Y. Park, J. H. Suh, Q.-V. Le, D. Kim, Y. B. Kim, G. H. Im, H. N. Kim, Y. S. Choe, J. Cho, S. Kim, and Y.-K. Oh, J. Controlled Release **327**, 616–626 (2020).
[160]L. Li, K. Dai, J. Li, Y. Shi, Z. Zhang, T. Liu, X. Jun, Z. Ruiping, and Z. Liu, Biomaterials **268**, 120587 (2021).
[161]Z. Fu, G. R. Williams, S. Niu, J. Wu, F. Gao, X. Zhang, Y. Yang, Y. Li, and L. M. Zhu, Nanoscale **12**(27), 14739–14750 (2020).
[162]Y. Qian, Y. Xu, Z. Yan, Y. Jin, X. Chen, W.-E. Yuan, and C. Fan, Nano Energy **83**, 105779 (2021).
[163]X. Xie, Z. Hou, G. Duan, S. Zhang, H. Zhou, Z. Yang, and R. Zhou, Colloids Surf., B **203**, 111765 (2021).
[164]X. Chen, P. Wu, M. Rousseas, D. Okawa, Z. Gartner, A. Zettl, and C. R. Bertozzi, J. Am. Chem. Soc. **131**(3), 890–891 (2009).
[165]Y. Zhang, C. Chan, Z. Li, J. Ma, Q. Meng, C. Zhi, H. Sun, and J. Fan, Langmuir **35**(18), 6179–6187 (2019).
[166]M. Ikram, I. Jahan, A. Haider, J. Hassan, A. Ul-Hamid, M. Imran, J. Haider, A. Shahzadi, A. Shahbaz, and S. Ali, Appl. Nanosci. **10**(7), 2339–2349 (2020).
[167]M. Guan, L. Hao, L. Chen, F. Gao, S. Qiu, H. Zhou, H. Chen, and X. Zhou, ACS Sustainable Chem. Eng. **8**(40), 15120–15133 (2020).
[168]K. Y. Gudz, E. S. Permyakova, A. T. Matveev, A. V. Bondarev, A. M. Manakhov, D. A. Sidorenko, S. Y. Filippovich, A. V. Brouchkov, D. V. Golberg, S. G. Ignatov, and D. V. Shtansky, ACS Appl. Mater. Interfaces **12**(38), 42485–42498 (2020).
[169]S. W. Xiong, P. G. Fu, Q. Zou, L. Y. Chen, M. Y. Jiang, P. Zhang, Z. G. Wang, L. S. Cui, H. Guo, and J. G. Gai, ACS Appl. Mater. Interfaces **13**(1), 196–206 (2021).
[170]M. Kıvanç, B. Barutca, A. T. Koparal, Y. Göncü, S. H. Bostancı, and N. Ay, Mater. Sci. Eng.: C **91**, 115–124 (2018).
[171]J. Santos, M. Moschetta, J. Rodrigues, P. Alpuim, and A. Capasso, Front. Bioeng. Biotechnol. **9**, 612669 (2021).
[172]Y. Pan, H. Zheng, G. Li, Y. Li, J. Jiang, J. Chen, Q. Xie, D. Wu, R. Ma, X. Liu, S. Xu, J. Jiang, X. Cai, M. Gao, W. Wang, H. Zuilhof, M. Ye, and R. Li, ACS Nano **16**(5), 7674–7688 (2022).
[173]G. Aytoğu, Y. Goncu, B. N. Yaman, B. Kadiroğlu, Ö. Ateş, M. E. Üreyen, N. Ay, and K. Yeşilbağ, J. Boron **8**(2), 66–75 (2023).
[174]V. Vatanpour, B. Keskin, S. A. Naziri Mehrabani, H. Karimi, N. Arabi, A. H. Behroozi, A. Shokrollahi-far, B. Yavuzturk Gul, and I. Koyuncu, J. Environ. Chem. Eng. **10**(1), 107035 (2022).
[175]G. Peng and B. Fadeel, Adv. Drug Delivery Rev. **188**, 114422 (2022).
[176]Ö. Şen, M. Emanet, and M. Çulha, Front. Bioeng. Biotechnol. **6**, 83 (2018).
[177]N. Hammi, M. Kędzierska, N. Wrońska, N. Katir, J. Dhainaut, S. Royer, K. Lisowska, M. Bryszewska, K. Miłowska, and A. El Kadib, Mater. Adv. **4**(21), 5191–5199 (2023).
[178]A. Jayakumar, S. Mathew, S. Radoor, J. T. Kim, J.-W. Rhim, and S. Siengchin, Mater. Today Chem. **30**, 101492 (2023).
[179]N. Yapici, E. Chiari, X. Liu, C. Pilon, D. Gibbs, R. Oakley, D. Zhang, and Y. K. Yap, in Symposium NM01, 2024 Materials Research Society Fall Meeting, Paper *NM01.12.10, Boston, MA, December 1–6, 2024.
[180]Y. K. Yap, in Symposium NM01, 2024 Materials Research Society Fall Meeting, Paper *NM01.12.01, Boston, MA, December 1–6, 2024.
[181]J. S. Lee, S. H. Choi, S. J. Yun, Y. I. Kim, S. Boandoh, J.-H. Park, B. G. Shin, H. Ko, S. H. Lee, Y.-M. Kim, Y. H. Lee, K. K. Kim, and S. M. Kim, Science **362**(6416), 817–821 (2018).